

**Abstract**

**Measurement of total hadronic differential cross  
sections in the LArIAT experiment**

Elena Gramellini

2018

Abstract goes here. Limit 750 words.

# **Measurement of total hadronic differential cross sections in the LArIAT experiment**

A Dissertation  
Presented to the Faculty of the Graduate School  
of  
Yale University  
in Candidacy for the Degree of  
Doctor of Philosophy

by  
Elena Gramellini

Dissertation Director: Bonnie T. Fleming

Date you'll receive your degree

Copyright © 2017 by Elena Gramellini

All rights reserved.

# Contents

<b>Acknowledgements</b>	<b>xii</b>
<b>0 Introduction</b>	<b>1</b>
<b>1 The theoretical framework</b>	<b>2</b>
1.1 The Standard Model . . . . .	2
1.2 Neutrinos: tiny cracks in the Standard Model . . . . .	4
1.2.1 Neutrinos in the Standard Model . . . . .	4
1.2.2 Neutrino Oscillations . . . . .	6
1.2.3 Make up of Neutrino Interactions . . . . .	7
1.3 Beyond the Standard Model . . . . .	13
1.3.1 Open Questions in Neutrino Physics . . . . .	13
1.3.2 Towards a more fundamental theory: GUTs . . . . .	17
1.4 Motivations for Hadronic Cross Sections in Argon . . . . .	18
1.4.1 Pion-Argon Total Hadronic Cross Section . . . . .	18
1.4.2 Kaon-Argon Total Hadronic Cross Section . . . . .	19
<b>2 Liquid Argon Detectors at the Intensity Frontier</b>	<b>24</b>
2.1 Liquid Argon Time Projection Chambers at the Intensity Frontier . .	25
2.1.1 Time Projection Chamber . . . . .	25
2.1.2 Ionization Detectors with Noble Liquids . . . . .	25

2.1.3	LArTPC: Principles of Operation . . . . .	25
2.1.4	Liquid Argon Ionization Charge Detection . . . . .	25
2.1.5	Liquid Argon scintillation Light Detection . . . . .	25
2.2	The SBN Program: Neutrino Interaction and Detection . . . . .	25
2.3	DUNE: Rare Decay Searches . . . . .	25
2.4	Enabling the next generation of discoveries: LArIAT . . . . .	27
<b>3</b>	<b>LArIAT: Liquid Argon In A Testbeam</b>	<b>29</b>
3.1	The Particles Path to LArIAT . . . . .	29
3.2	LArIAT Tertiary Beam Instrumentation . . . . .	32
3.2.1	Bending Magnets . . . . .	32
3.2.2	Multi-Wire Proportional Chambers . . . . .	34
3.2.3	Time-of-Flight System . . . . .	36
3.2.4	Punch-Through and Muon Range Stack Instruments . . . . .	37
3.2.5	LArIAT Cosmic Ray Paddle Detectors . . . . .	39
3.3	In the Cryostat . . . . .	40
3.3.1	Cryogenics and Argon Purity . . . . .	40
3.3.2	LArTPC: Charge Collection . . . . .	43
3.3.3	LArTPC: Light Collection System . . . . .	46
3.4	Trigger and DAQ . . . . .	49
3.5	Control Systems . . . . .	50
<b>4</b>	<b>Hadron Interactions in Argon: Cross Section</b>	<b>56</b>
4.1	How to Measure a Hadron Cross Section in LArIAT . . . . .	56
4.1.1	Event Selection . . . . .	57
4.1.2	Wire Chamber to TPC Match . . . . .	59
4.1.3	The Thin Slice Method . . . . .	60
4.1.4	Procedure testing with truth quantities . . . . .	63

<b>5 Samples Preparation</b>	<b>66</b>
5.1 LArIAT Data . . . . .	66
5.2 LArIAT Monte Carlo . . . . .	66
5.2.1 G4Beamline . . . . .	66
5.2.2 Data Driven MC . . . . .	66
5.3 Energy Calibration . . . . .	66
5.4 Tracking Studies . . . . .	66
5.4.1 Selection Study for the Wire Chamber to TPC Match . . . . .	67
5.4.2 Interaction Point Optimization . . . . .	70
5.4.3 Tracking spatial and angular resolution . . . . .	71
<b>6 Background subtraction</b>	<b>72</b>
6.1 Assessing Beamline Contamination . . . . .	72
6.1.1 Electron and Muon contamination . . . . .	72
6.1.2 Contamination from secondaries . . . . .	74
6.2 Subtraction . . . . .	74
6.3 Capture and decay . . . . .	75
<b>7 Negative Pion Cross Section Measurement</b>	<b>79</b>
<b>8 Uncertainty budget</b>	<b>80</b>
8.1 Pure beam of pions . . . . .	80
8.1.1 Uncertainty on $E_{Beam}^{kin}$ . . . . .	81
8.1.2 Uncertainty on $E_{loss}$ . . . . .	81
8.1.3 Uncertainty on dE/dx and pitch . . . . .	82
8.1.4 Uncertainty on track end, aka efficiency correction . . . . .	82
<b>A Measurement of LArIAT Electric Field</b>	<b>84</b>

# List of Figures

1.1	Feynman diagrams for proton decay “golden modes”: $p \rightarrow K^+ \bar{\nu}$ for supersymmetric GUTs on the left and $p \rightarrow e^+ \pi^0$ for gauge-mediated GUTs on the right. . . . .	20
1.2	Ratios between experimental and calculated cross sections as from [23]. Top: Total cross sections. Bottom: reaction cross sections. . . . .	23
1.3	Total $K^+$ and $K^-$ cross sections on carbon as from [9]. . . . .	23
1.4	total hadronic cross section for carbon implemented in Geant4 10.01.p3 with overlaid with the Bugg and Frideman data. . . . .	23
2.1	Proton decay lifetime limits from passed and future experiments. . . . .	26
2.2	Momentum of the kaon outgoing a proton decay event as simulated by the Genie 2.8.10 event generator in argon. The red line represent the kaon momentum distribution before undergoing the simulated final state interaction inside the argon nucleus, while the blue line represents the momentum distribution after FSI. . . . .	27
3.1	Layout of Fermilab Accelerator complex. . . . .	31
3.2	Bird’s eye view of the LArIAT tertiary beamline. In grey: upstream and downstream collimators; in yellow: bending magnets; in red: wire chambers; in blue: time of flight; in green: liquid argon TPC volume; in maroon: muon range stack. . . . .	31

3.3	Magnetic field over current as a function of the current, for one NDB magnet (excitation curve). The data was collected using two hall probes (blue and green). We fit the readings with a cubic function (black) to average of measurements (red) given in the legend. . . . .	33
3.4	One of the four Multi Wire Proportional Chambers (WC) used in the LArIAT tertiary beamline and relative read-out electronics. . . . .	34
3.5	Image of the down stream time of flight paddle, PMTs and relative support structure before mounting. . . . .	38
3.6	Photograph of one of the scintillation counters used in the cosmic towers. . . . .	40
3.7	Left: the LArIAT TPC in the inner volume of the open cryostat. Right: cryostat fully sealed ready to be transported to FTBF. . . . .	41
3.8	Main modifications to the ArgoNeuT cryostat: 1) outlet for connection to the purification system at the bottom of the cryostat; 2) the “beam-window” on the outer endcap and “excluder” which reduce the amount of non-instrumented material before the TPC; 3) the side port to host the light collection system. . . . .	42
3.9	Schematic of the LArIAT high voltage system. . . . .	44
3.10	Schematic of the three drift regions inside the LArIAT TPC: the main drift volume between the cathode and the shield plane (C-S) in green, the region between the shield plane and the induction plane (S-I) in purple, and the region between the induction plane and the collection plane (I-C) in pink. . . . .	45
3.11	Overview of LArIAT Front End electronics. . . . .	47
3.12	LArIAT’s photodetector system for observing LAr scintillation light inside the TPC (left), and a simplified schematic of VUV light being wavelength-shifting along the TPB-coated reflecting foils (right). . . . .	48

3.13	Interface of the Synoptic slow control system . . . . .	51
3.14	Beam position at the upstream wire chambers monitored with ACNET. .	52
3.15	Run Status page at LArIAT downtime. At the top the yellow bar displays the current position in the Fermilab supercycle. Interesting information to be monitored by the shifter were the run number and number of spills, time elapsed from data taking (here in red), the energy of the secondary beam and the trigger paths. . . . .	54
3.16	High occupancy event display: induction plane (top) and collection plane (bottom). . . . .	55
4.1	The mass plotted for a sample of Run-II events reconstructed in the beamline, negative polarity runs on the left and positive polarity runs on the right. The classification of the events into $\pi$ , $\mu$ , $e$ , kaon, or proton is based on this distribution. <b>CHANGE PLOTS</b> . . . . .	58
4.2	Hadronic cross sections for $\pi^-$ -Ar (left) and $K^+$ -Ar (right) implemented in Geant4 10.01.p3 (solid lines) overlaid the true MC cross section as obtained with the sliced TPC method (markers). The total cross section is shown in green, the elastic cross section in blue and the inelastic cross section in red. . . . .	65
5.1	Efficiency (left) and purity (right) for wire chamber-to-TPC match as a function of the radius and angle selections. . . . .	70
6.1	Beam composition for the -60A runs (left) and -100A runs (right). The solid blue plot represents the pion content, the yellow plot represents the muon content and the grey plot represents the electron content. The plots are area normalized to the number of data events, shown in red. . . . .	73

6.2 A graphical rendering of the beamline contamination background subtraction. The contribution of the contaminants is shown in green for the secondaries, in orange for the muons and in pink for electrons. The colored plots are coming from the MC and are staggered. The percentages shown in the legend are the percentages of contaminants over the total number of events passing the selection chain. We actually expect way less contamination. . . . .	75
6.3 True momentum distribution at wire chamber 4 for every simulated pion arriving in the TPC (pink), ending its life in capture (green) or in decay (blue) in the TPC, linear vertical axis on the left, logarithmic on the right. . . . .	76
6.4 Survival ratio as a function of selection threshold on true momentum at wire chamber four for every simulated pion arriving in the TPC (pink), capture (green) or in decay (blue). . . . .	78
6.5 Ratio between the capture (green) and decay (blue) events over the total number of events as a function of the true momentum at wire chamber four. . . . .	78
A.1 Drift velocity dependence on electric field for several temperatures. The slope of the line at any one point represents the electron mobility for that given temperature and electric field. . . . .	85
A.2 <b>get rid of current line</b> LArIAT HV simple schematics. . . . .	86
A.3 <b>the axis is wrong!!</b> Current reading from the Glassman between May 25th and May 30th, 2016 (typical Run-II conditions). . . . .	86
A.4 Pictorial representation of the YX view of the TPC. The distance within the anode planes and between the shield plane and the cathode is purposely out of proportion to illustrate the time difference between hits on collection and induction. A ACP track is shown as an example.	90

A.5	Angle definition in the context of LArIAT coordinates system. . . . .	90
A.6	Collection plane $\Delta t$ fit for Run II positive polarity ACP data selected tracks. . . . .	91
A.7	Induction plane $\Delta t$ fit for Run II positive polarity ACP data selected tracks. . . . .	91

# List of Tables

1.1	SM elementary fermions. The subscripts L and R indicate respectively the negative helicity (left-handed) and the positive helicity (right-handed).	3
1.2	Summary of experimental results on neutrino oscillation parameters.	
	<b>ADD CITATIONS</b>	<b>7</b>
3.1	Cathode and anode planes default voltages	46
6.1	Beamline composition per magnet settings	73
6.2	Data events per magnet settings	74
8.1	Back of the envelope calculation	82
A.1	Electric field and drift velocities in LArIAT smaller drift volumes	85
A.2	$\Delta t$ for the different data samples used for the Anode-Cathode Piercing tracks study.	90

# Acknowledgements

A lot of people are awesome, especially you, since you probably agreed to read this when it was a draft.

# **Chapter 0**

## **Introduction**

# Chapter 1

## The theoretical framework

### 1.1 The Standard Model

The Standard Model (SM) of particle physics is the most accurate theoretical description of the subatomic world and, in general, one of the most precisely tested theories in the history of physics. The SM describes the strong, electromagnetic and weak interactions among elementary particles in the framework of quantum field theory, accounting for the unification of electromagnetic and weak interactions for energies above the vacuum expectation value of the Higgs field. The SM does not describe gravity or general relativity.

The Standard Model is a gauge theory based on the local group of symmetry

$$G_{SM} = SU(3)_C \otimes SU(2)_T \otimes U(1)_Y \quad (1.1)$$

where the subscripts indicate the conserved charges: the strong charge, or color C, the weak isospin T (or rather its third component T<sub>3</sub>) and the hypercharge Y. These quantities can be related to the electric charge Q through the Gell-Mann-Nishijima relation:

$$Q = \frac{Y}{2} + T_3. \quad (1.2)$$

Generation	I	II	III	T	Y	Q
Leptons	$\begin{pmatrix} \nu_e \\ e \end{pmatrix}_L$	$\begin{pmatrix} \nu_\mu \\ \mu \end{pmatrix}_L$	$\begin{pmatrix} \nu_\tau \\ \tau \end{pmatrix}_L$	$1/2$ $-1/2$	$-1$ $-1$	$0$ $-1$
	$e_R$	$\mu_R$	$\tau_R$	0	-2	1
Quarks	$\begin{pmatrix} u \\ d' \end{pmatrix}_L$	$\begin{pmatrix} c \\ s' \end{pmatrix}_L$	$\begin{pmatrix} t \\ b' \end{pmatrix}_L$	$1/2$ $-1/2$	$1/3$ $1/3$	$2/3$ $-1/3$
	$u_R$ $d'_R$	$c_R$ $s'_R$	$t_R$ $b'_R$	0 0	$4/3$ $-2/3$	$2/3$ $-1/3$

Table 1.1: SM elementary fermions. The subscripts L and R indicate respectively the negative helicity (left-handed) and the positive helicity (right-handed).

In the quantum field framework, the elementary particles correspond to the irreducible representations of the  $G_{SM}$  symmetry group. In particular, the particles are divided in two categories, fermions and bosons, according to their spin-statistics. Described by the Fermi-Dirac statistics, fermions have half-integer spin and are sometimes called “matter-particles”. Bosons or “force carriers” have integer spin, follow the Bose-Einstein statistics and mediate the interaction between fermions. The fundamental fermions and their quantum numbers are listed in Tab 1.1.

Quarks can interact via all three the fundamental forces; they are triplets of  $SU(3)_C$ , that is they can exist in three different colors: C = R, G, B. If one chooses a base where  $u$ ,  $c$  and  $t$  quarks are simultaneously eigenstates of both the strong and the weak interactions, the remaining eigenstates are usually written as  $d$ ,  $s$  and  $b$  for the strong interaction and  $d'$ ,  $s'$  and  $b'$  for the weak interaction, because the latter ones are the result of a Cabibbo rotation on the first ones. Charged leptons interact via the weak and the electromagnetic forces, while neutrinos only interact via the weak force. The gauge group univocally determines the number of gauge bosons that carry the interaction; the gauge bosons correspond to the generators of

the group: eight gluons (g) for the strong interaction, one photon ( $\gamma$ ) and three bosons ( $W^\pm$ ,  $Z^0$ ) for the electroweak interaction. A gauge theory by itself can not provide a description of massive particles, but it is experimentally well known that most of the elementary particles have non-zero masses. The introduction of massive fields in the Standard Model lagrangian would make the theory non-renormalizable, and - so far - mathematically impossible to handle. This problem is solved in the Standard Model by the introduction of a scalar iso-doublet  $\Phi(x)$ , the Higgs field, which gives mass to  $W^\pm$  and  $Z^0$  gauge bosons through the electroweak symmetry breaking and to the fermions through Yukawa coupling [27, 28]. The discovery of the Higgs boson in 2012 by the LHC experiments [11, 12] marked the ultimate confirmation of a long history of Standard Model successful predictions.

## 1.2 Neutrinos: tiny cracks in the Standard Model

### 1.2.1 Neutrinos in the Standard Model

Neutrino were introduced in the SM as left-handed massless Weyl spinors. The Dirac equation of motion

$$(i\gamma^\mu \partial_\mu - m)\psi = 0 \quad (1.3)$$

for a fermionic field

$$\psi = \psi_L + \psi_R \quad (1.4)$$

is equivalent to the equaitons

$$i\gamma^\mu \partial_\mu \psi_L = m\psi_R \quad (1.5)$$

$$i\gamma^\mu \partial_\mu \psi_R = m\psi_L \quad (1.6)$$

for the chiral fields  $\psi_R$  and  $\psi_L$ , whose evolution in space and time is coupled through the mass  $m$ . If the fermion is massless, the chiral fields decouple and the

fermion can be described by a single Weyl spinor with two independent components [38]. Pauli initially rejected the description of a physical particle through a single Weyl spinor because of its implication of parity violation. In fact, since the spatial inversion operator throws  $\psi_R \leftrightarrow \psi_L$ , parity is conserved only if the both the chiral components exist at the same time. For the neutrino introduction in the SM, experiments came in help of the theoretical description. The constraint of parity conservation weakened after Wu's experiment in 1957 [39]. Additionally, there was no experimental indication for massive neutrinos nor evidence of interaction via the neutrino right-handed component.

The symmetry group  $SU(2)_T \otimes U(1)_Y$  is the only group relevant for neutrino interactions. The SM electroweak lagrangian is the most general renormalizable lagrangian invariant under the local symmetry group  $SU(2)_T \otimes U(1)_Y$ . The lagrangian couples the weak isotopic spin doublets and singlets described in 1.1 with the gauge bosons  $A_a^\mu$  ( $a = 1, 2, 3$ ) and  $B^\mu$ , and Higgs doublet  $\Phi(x)$ :

$$\begin{aligned}
\mathcal{L} = & i \sum_{\alpha=e,\mu,\tau} \bar{L}'_{\alpha L} \not{D} L'_{\alpha L} + i \sum_{\alpha=1,2,3} \bar{Q}'_{\alpha L} \not{D} Q'_{\alpha L} \\
& + i \sum_{\alpha=e,\mu,\tau} \bar{l}'_{\alpha R} \not{D} l'_{\alpha R} + i \sum_{\alpha=d,s,b} \bar{q}'^D_{\alpha R} \not{D} q'^D_{\alpha R} + i \sum_{\alpha=u,c,t} \bar{q}'^U_{\alpha R} \not{D} q'^U_{\alpha R} \\
& - \frac{1}{4} A_{\mu\nu} A^{\mu\nu} - \frac{1}{4} B_{\mu\nu} B^{\mu\nu} \\
& + (D_\rho \Phi)^\dagger (D^\rho \Phi) - \mu^2 \Phi^\dagger \Phi - \lambda (\Phi^\dagger \Phi)^2 \\
& - \sum_{\alpha,\beta=e,\mu,\tau} \left( Y_{\alpha\beta}^n \bar{L}'_{\alpha L} \Phi l'_{\beta R} + Y_{\alpha\beta}^{n*} \bar{l}'_{\beta R} \Phi^\dagger L'_{\alpha L} \right) \\
& - \sum_{\alpha=1,2,3} \sum_{\beta=d,s,b} \left( Y_{\alpha\beta}^D \bar{Q}'_{\alpha L} \Phi q'^D_{\beta R} + Y_{\alpha\beta}^{D*} \bar{q}'^D_{\beta R} \Phi^\dagger Q'_{\alpha L} \right) \\
& - \sum_{\alpha=1,2,3} \sum_{\beta=u,c,t} \left( Y_{\alpha\beta}^U \bar{Q}'_{\alpha L} \tilde{\Phi} q'^U_{\beta R} + Y_{\alpha\beta}^{U*} \bar{q}'^U_{\beta R} \tilde{\Phi}^\dagger Q'_{\alpha L} \right). \tag{1.7}
\end{aligned}$$

The first two lines of the lagrangian summarize the kinetic terms for the fermionic

fields and their coupling to the gauge bosons  $A_a^{\mu\nu}$ ,  $B^{\mu\nu}$ <sup>1</sup>. The third line describes the kinetic terms and the self-coupling terms of the gauge bosons. The forth line is the Higgs lagrangian, which results in the spontaneous symmetry breaking. The last three lines describe the Yukawa coupling between fermions and the Higgs field, origin of the fermion's mass.

The coupling between left-handed and right-handed field generates the mass term for fermions. The SM assumes only left-handed components for neutrinos, thus implying zero neutrino mass. Since any linear combination of massless fields results in a massless field, the flavor eigenstates are identical to the mass eigenstates in the SM.

### 1.2.2 Neutrino Oscillations

The determination of the flavor of a neutrino dynamically arises from the corresponding charged lepton associated in a change current interaction; for example, a  $\nu_e$  is a neutrino which produces an  $e^-$ , a  $\bar{\nu}_\mu$  is a neutrino which produces a  $\mu^+$ , *etc.* The neutrino flavor eigenstates  $|\nu_\alpha\rangle$ , with  $\alpha = e, \mu, \tau$ , are orthogonal to each other and form a base for the the weak interaction matrix.

Overwhelming experimental data show neutrinos change flavor during their propagation [34]. This phenomenon, called “neutrino oscillations”, was predicted first by Bruno Pontecorvo in 1957 [35]. Neutrino oscillations are possible only if the neutrino flavor eigenstate are not identical to the mass eigenstates, thus resulting in the first evidence of physics beyond the Standard Model. A minimal extension of the Standard Model introduces three mass eigenstates,  $|\nu_i\rangle$  ( $i = 1, 2, 3$ ), whose mass  $m_i$  is well defined. The unitary Pontecorvo-Maki-Nakagawa-Sakata matrix transforms the spinor wave functions ( $\psi$ ) of each component between flavor and mass bases as follows

---

1. In gauge theories the ordinary derivative  $\partial_\mu$  is substituted with the covariant derivative  $D_\mu$ . Here  $D_\mu = \partial_\mu + igA_\mu \cdot I + ig'B_\mu \frac{Y}{2}$ , where I and Y are the SU(2)<sub>L</sub> and U(1)<sub>Y</sub> generators, respectively.

$$\sum \psi_\alpha |\nu_\alpha\rangle = \sum \psi_i |\nu_i\rangle, \rightarrow \psi_\alpha = U_{PMNS} \psi_i, \quad (1.8)$$

with

$$U_{PMNS} = \begin{bmatrix} c_{12} & s_{12} & 0 \\ -s_{12} & c_{12} & 0 \\ 0 & 0 & 1 \end{bmatrix} \begin{bmatrix} c_{13} & 0 & s_{13}e^{-i\delta} \\ 0 & 1 & 0 \\ -s_{13}e^{-i\delta} & 0 & c_{13} \end{bmatrix} \begin{bmatrix} 1 & 0 & 0 \\ 0 & c_{23} & s_{23} \\ 0 & -s_{23} & c_{23} \end{bmatrix} \begin{bmatrix} e^{i\alpha_1} & 0 & 0 \\ 0 & e^{i\alpha_2} & 0 \\ 0 & 0 & 1 \end{bmatrix} \quad (1.9)$$

where  $c$  e  $s$  stand respectively for cosine and sine of the corresponding mixing angles ( $\theta_{12}$ ,  $\theta_{23}$  and  $\theta_{13}$ ),  $\delta$  is the Dirac CP violation phase,  $\alpha_1$  and  $\alpha_2$  is the eventual Majorana CP violation phases. Experimental results on neutrino oscillations are generally reported in terms of the mixing angles and of the squared mass splitting  $\Delta m_{ab}^2 = m_a^2 - m_b^2$ , where  $a$  and  $b$  represent the mass eigenstates. A summary of the current status of experimental results, albeit partial, is given in table 1.2.

Table 1.2: Summary of experimental results on neutrino oscillation parameters. **ADD CITATIONS**

	Value	Precision	Experiment
$\theta_{23}$	$45^\circ$	9.0%	Super Kamiokande, MINOS,
$\Delta m_{23}^2$	$2.5 \cdot 10^{-3} \text{ eV}^2$	1.8%	No $\nu$ a, MACRO
$\theta_{12}$	$34^\circ$	5.8%	SNO, Gallex,
$\Delta m_{12}^2$	$7.4 \cdot 10^{-5} \text{ eV}^2$	2.8%	SAGE, KamLAND
$\theta_{13}$	$9^\circ$	4.7%	DAYA Bay,
$\Delta m_{13}^2$	$2.5 \cdot 10^{-3} \text{ eV}^2$	1.8%	RENO

### 1.2.3 Make up of Neutrino Interactions

All neutrino experiments involving the detection of single neutrinos are concerned with neutrino interactions (and neutrino cross sections) on nuclei. Given the invisible nature of neutrinos, characterizing the products of their interaction is the only method

to assess their flavor and eventually reconstruct their energy. In real life experiments, this task is complicated by the structure of the nucleus. Nuclear effects modify the kinematic and final state of the neutrino interaction products and are particularly relevant in modern neutrino experiments that use fairly heavy nuclear targets to increase their event yields.

Data on neutrino scattering off many different nuclei are available for both charged current (CC) and neutral current (NC) channels, as summarized here [22]. oscillation worth it: Sam

his work summarizes accelerator-based neutrino cross section measurements performed in the  $\sim 0.1 \text{--} 300 \text{ GeV}$  range with an emphasis on inclusive, quasi-elastic, and pion production processes, areas where we have the most experimental input at present (Table 49.1 and Table 49.2). For a more comprehensive discussion of neutrino cross sections, including neutrino-electron elastic scattering and lower energy neutrino measurements, the reader is directed to a recent review of this subject [1]. Here, we survey existing experimental data on neutrino interactions and do not attempt to provide a census of the associated theoretical calculations, which are both important and plentiful.

Inclusive Scattering Over the years, many experiments have measured the total inclusive cross section for neutrino ( $\nu N \rightarrow X$ ) and antineutrino ( $\bar{\nu} N \rightarrow X$ ) scattering off nucleons covering a broad range of neutrino energies. As can be seen in Fig. 49.1, the inclusive cross section approaches a linear dependence on neutrino energy. Such behavior is expected for point-like scattering of neutrinos from quarks, an assumption which breaks down at lower energies. To provide a more complete picture, differential cross sections for such inclusive scattering processes have been reported ? these include measurements on iron from NuTeV [42] and, more recently, at lower neutrino energies on argon from ArgoNeuT [2,3] and on carbon from T2K [37]. MINERvA has also provided new measurements of the ratios of the muon neutrino CC

inclusive scattering cross section on a variety of nuclear targets such as lead, iron, and carbon [11]. At high energy, the inclusive cross section is dominated by deep inelastic scattering (DIS). Several high energy neutrino experiments have measured the DIS cross sections for specific final states, for example opposite-sign dimuon production. The most recent dimuon cross section measurements include those from CHORUS [43], NOMAD [44], and NuTeV [45]. At lower neutrino energies, the inclusive cross section is an additionally complex combination of quasi-elastic scattering

Quasi-elastic scattering Quasi-elastic (QE) scattering is the dominant neutrino interaction for neutrino energies less than  $\sim 1$  GeV and represents a large fraction of the signal samples in many neutrino oscillation experiments. Historically, neutrino (antineutrino) quasi-elastic scattering refers to the process,  $\nu \rightarrow n \rightarrow p (\bar{\nu} \rightarrow p \rightarrow n)$ , where a charged lepton and single nucleon are ejected in the elastic interaction of a neutrino (or antineutrino) with a nucleon in the target material. This is the final state one would strictly observe, for example, in scattering off of a free nucleon target. Fig. 49.2 displays the current status of existing measurements of  $\nu$  and  $\bar{\nu}$  QE scattering cross sections as a function of neutrino energy. In this plot, and all others in this review, the prediction from a representative neutrino event generator (NUANCE) [46] provides a theoretical comparator. Other generators and more sophisticated calculations exist which can yield significantly different predictions [47]. Note that modern experiments have recently opted to report QE cross sections as a function of final state muon or proton kinematics [17,18,48]. Such distributions are more difficult to compare between experiments but are much less model-dependent and provide more stringent tests of the theory than cross sections as a function of neutrino energy ( $E_\nu$ ) or 4-momentum transfer ( $Q^2$ ).

In many of these initial measurements of the neutrino QE cross section, bubble chamber experiments employed light targets (H<sub>2</sub> or D<sub>2</sub>) and required both the detection of the final state muon and single nucleon; thus the final state was clear and

elastic kinematic conditions could be verified. The situation is more complicated, of course, for heavier nuclear targets. In this case, nuclear effects can impact the size and shape of the cross section as well as the final state kinematics and topology. Due to intranuclear hadron rescattering and the possible effects of correlations between target nucleons, additional nucleons may be ejected in the final state; hence, a QE interaction on a nuclear target does not always imply the ejection of a single nucleon. One therefore needs to take some care in defining what one means by neutrino QE scattering when scattering off targets heavier than H2 or D2. Adding to the complexity, recent MiniBooNE measurements of the ?? and ?? QE scattering cross sections on carbon near 1 GeV have revealed a significantly larger cross section than originally anticipated [17,18]. Such an enhancement was observed many years prior in electron-nucleus scattering [57] and is believed to be due to the presence of correlations between target nucleons in the nucleus. As a result, the impact of such nuclear effects on neutrino QE scattering has recently been the subject of intense experimental and theoretical scrutiny with potential implications on event rates, nucleon emission, neutrino energy reconstruction, and neutrino/antineutrino ratios. The reader is referred to a recent review of the situation in [58,59]. Additional measurements are clearly needed before a complete understanding is achieved. To help drive further progress, neutrino-nucleus QE cross sections have been reported for the first time in the form of double-differential distributions in muon kinematics,  $d^2\sigma/dT\cos\theta$ , by MiniBooNE [17,18] thus reducing the model-dependence of the reported data and allowing a more rigorous two-dimensional test of the underlying nuclear theory. Experiments such as ArgoNeuT have begun to provide the first measurements of proton multiplicities in neutrino-argon QE scattering [4,48], a critical ingredient in understanding the hadronic side of these interactions and final state effects. MINOS, NOvA, and T2K have started to study QE interactions in their near detectors with sizable statistics [29,39,60]. Most recently, MINERvA has mea-

sured the differential cross section,  $d\sigma/dQ^2QE$ , ?e QE scattering [61], single proton emission [14], and vertex energy in both ?? and ?? QE interactions in hydrocarbon [12,13]. With the MiniBooNE results having revealed additional complexities in the QE channel, measurements from other neutrino experiments are crucial for getting a better handle on the underlying nuclear physics impacting neutrino-nucleus interactions. What we once thought was ?simple? QE scattering is in fact not so simple. In addition to such charged current investigations, measurements of the neutral current counterpart of this channel have also been performed. The most recent NC elastic scattering cross section measurements include those from BNL E734 [62], MiniBooNE [20,21,22], and T2K [40]. A number of measurements of the Cabibbo-suppressed antineutrino QE hyperon production cross section have additionally been reported [56,63], although not in recent years.

**Pion Production** In addition to such elastic processes, neutrinos can also inelastically scatter producing a nucleon excited state (? N?). Such baryonic resonances quickly decay, most often to a nucleon and single-pion final state. Historically, experiments have measured various exclusive final states associated with these reactions, the majority of which have been on hydrogen and deuterium targets [1]. In addition to such resonance production processes, neutrinos can also coherently scatter off of the entire nucleus and produce a distinctly forward-scattered single pion final state. Both CC( $\nu\nu A\rightarrow A\pi^+ + \bar{\nu}\nu A\rightarrow A\pi^- + \bar{\nu}$ ) and NC( $\nu\nu A\rightarrow A\pi^0 + \bar{\nu}\nu A\rightarrow A\pi^0$ ) processes are possible in this case. Even though the level of coherent pion production is small compared to resonant processes, observations exist across a broad energy range and on multiple nuclear targets [64]. More recently, several modern neutrino experiments have measured coherent pion production cross sections including ArgoNeuT [5], K2K [8], MINERvA [15], MiniBooNE [27], MINOS [65], NOMAD [32], and SciBooNE [34,36]. As with QE scattering, a new appreciation for the significance of nuclear effects has surfaced in pion production channels, again due to the use of heavy nuclear

targets in modern neutrino experiments. Many experiments have been careful to report cross sections for various detected final states, thereby not correcting for large and uncertain nuclear effects (e.g., pion rescattering, charge exchange, and absorption) which can introduce unwanted sources of uncertainty and model dependence. Recent measurements of single-pion cross sections, as published by K2K [9,10], MiniBooNE [24], and SciBooNE [35], take the form of ratios with respect to QE or CC inclusive scattering samples. Providing the most comprehensive survey of neutrino single-pion production to date, MiniBooNE has recently published a total of 16 single- and double-differential cross sections for both the final state muon (in the case of CC scattering) and pion in these interactions; thus, providing the first measurements of these distributions (Fig. 49.3) [23?26]. MINERvA has recently produced similar kinematic measurements at higher neutrino energies (Fig. 49.4) [16,66]. Regardless of the interaction channel, such differential cross section measurements (in terms of observed final state particle kinematics) are now preferred for their reduced model dependence and for the additional kinematic information they provide. Such a new direction has been the focus of modern measurements as opposed to the reporting of more model-dependent, historical cross sections as a function of  $E_\nu$  or  $Q^2$ . Together with similar results for other interaction channels, a better understanding and modeling of nuclear effects will be possible moving forward. It should be noted that baryonic resonances can also decay to multi-pion, other mesonic ( $K, \pi, \eta$ , etc.), and even photon final states. Experimental results for these channels are typically sparse or non-existent [1]; however, photon production processes can be an important background for  $\nu e \rightarrow \nu e$  appearance searches and thus have become the focus of some recent experimental investigations; for example, in NOMAD [67].

## 1.3 Beyond the Standard Model

The discovery of neutrino oscillation and its implication of non-zero neutrino mass mark the beginning of a new, exciting era in neutrino physics: the era of physics Beyond the Standard Model (BSM) at the intensity frontier. We are currently searching for new, deeper theories that can accommodate neutrinos with tiny but non-zero masses, while remaining consistent with the rest of the Standard Model.

### 1.3.1 Open Questions in Neutrino Physics

On one hand, the last three decades of experiments in neutrino oscillations brought spectacular advancements in the understanding of the oscillations pattern, measuring the neutrino mixing angles and mass splitting with a precision of less than 10%. On the other, it opened the field for a series of questions needing experimental answers.

**Sterile neutrinos.** Hints to the existence of at least one additional neutrino, in the form of various anomalies, have been puzzling physicists almost from the beginning of neutrino oscillation searches. Originally designed to look for evidence of neutrino oscillation, the Liquid Scintillator Neutrino Detector (LSND) [17] provided a first conflicting result with the Standard Model expectation of only three neutrino flavors. A second conflicting result has also been provided by the MiniBooNE experiment [15]. The LSND and MiniBooNE  $\nu_e$  and  $\bar{\nu}_e$  appearance results, known as the “LSND and MiniBooNE anomalies” [3, 4, 6], may be interpreted under the assumption of a new right-handed neutrino. The additional neutrino needs to be “sterile”, i.e needs not to couple with the electroweak force carriers, in order to meet the constraint imposed by the measurement of the width of the Z boson [1]. The new sterile neutrino would mainly be composed of a heavy neutrino  $\nu_4$  with mass  $m_4$  such that  $m_1, m_2, m_3 \ll m_4$  and  $\Delta m^2 = \Delta m_{14}^2 \sim [0.1 - 10] \text{ eV}^2$ . The introduction of sterile neutrinos is an appealing line of thinking, since this renormalizable generalization

of the Standard Model has the potential to impact long standing questions in high energy physics and cosmology: light sterile neutrinos are candidates for dark matter particles and there are ideas that the theory could be adjusted to explain the baryon asymmetry of the Universe via leptogenesis [25].

**CP Violation In Lepton Sector.** The measurement of non-zero value for the oscillation parameter  $\theta_{13}$  allows the exploration of low-energy CP violation in the lepton sector at neutrino long baseline oscillation experiments, enabling the possibility to measure the Dirac CP-violating phase  $\delta$ . Exciting theoretical results tie  $\delta$  directly to the generation of the baryon asymmetry of the Universe at the Grand Unified Theory scale [a couple of cit would be nice](#). According to the theoretical model described in [33], for example, leptogenesis can be achieved if  $|\sin \theta_{13} \sin \delta| > 0.11$ , i.e.  $\sin \delta > 0.7$ .

The asymmetry in the oscillation probability of neutrinos and antineutrinos is the observable sensitive to the Dirac CP-violating phase  $\delta$  leveraged in neutrino oscillation experiments. Using the parameterization of the PMNS matrix shown in Equation 1.9, the difference in the probability of  $\nu_e \rightarrow \nu_\mu$  oscillation and the probability of  $\bar{\nu}_e \rightarrow \bar{\nu}_\mu$  oscillation can be parametrized as follows [10],

$$P_{\nu_e \rightarrow \nu_\mu} - P_{\bar{\nu}_e \rightarrow \bar{\nu}_\mu} = J \cos \left( \pm \delta - \frac{\Delta_{31} L}{2} \right) \sin \left( \frac{\Delta_{21} L}{2} \right) \sin \left( \frac{\Delta_{31} L}{2} \right) \quad (1.10)$$

where

$$J = \cos \theta_{13} \sin 2\theta_{13} \sin 2\theta_{12} \sin 2\theta_{23} \quad (1.11)$$

is the Jarlskog invariant [29],  $L$  the neutrino baseline and  $\Delta_{ab}$  a factor proportional to the sign and magnitude of the mass splitting. From these equations, it is clear how the relative large value of  $\theta_{13}$  is a happy accident necessary not to completely suppress the sensitivity to CP violation. The equations also show how the sensitivity to  $\delta$  is tied to the measurement of the least precisely measured mixing angle,  $\theta_{23}$  (via

the  $\sin 2\theta_{23}$  term) and to an other unknown quantity, the neutrino “mass hierarchy” (via the  $\Delta_{ab}$  terms). The precise determination of  $\theta_{23}$  is often referred as to “the octant problem”. Current experimental results cite NOVA T2K are consistent with  $\theta_{23} = 45^\circ$ , which would imply maximal mixing between  $\nu_\mu - \nu_\tau$ , hinting to an intriguing new symmetry. Therefore, a precise measurement of  $\theta_{23}$  is of great interest for theoretical models of quark-lepton universality [59,84,85,86,87,88] , whose quark and lepton mixing matrices are proportional to the deviation of  $\theta_{23}$  from  $45^\circ$ .

**Neutrino mass hierarchy.** The “mass hierarchy” problem refers to the unknown ordering of the value of absolute mass of the neutrino mass eigenstates. Current oscillation experiments are sensitive only to the magnitude of the mass splitting, but not to its sign. cite hints In a framework where the lightest neutrino mass (arbitrarily) corresponds to the first eigenstate  $m_1$ , it is unknown whether  $m_2 - m_1 < m_3 - m_1$  (Normal Hierarchy) or  $m_2 - m_1 > m_3 - m_1$  (Inverted Hierarchy). The mass hierarchy affects not only the sensitivity to CP violation searches in long baseline oscillation experiments, but also the sensitivity to determine whether neutrinos are Majorana particles in neutrinoless double beta decay experiments.

**Majorana or Dirac?** Evidence of neutrino oscillations demand the introduction in the theory of a mechanism which can give mass to the neutrinos. This mechanism should possibly also explain why neutrino masses are at least six orders of magnitude lower than the electron mass (the second lightest SM fermion). In a description of neutrinos as Dirac 4-component spinors, the neutrino field acquires mass via the Higgs mechanism as any other fermion of the SM. In this case, the neutrino mass is given by  $m_a = \frac{y_a^\nu v}{\sqrt{2}}$ , where  $v$  is the Higgs VEV and  $y_a^\nu$  is the Yukawa coupling between the Higgs and the neutrino. The smallness of neutrino masses can only be pinned on a tiny Yukawa coupling which is not justified by the theory.

In 1937, Majorana demonstrated that the introduction of a two components spinor is sufficient to describe a massive fermion [30]. The Dirac equations of motion for the

chiral fields (equations 1.5 and 1.6) hold true in the case of two components spinor under the assumption that the chiral components  $\psi_R$  and  $\psi_L$  are correlated through the charge conjugation matrix  $\mathcal{C}$ ,  $\psi_R = \mathcal{C}\bar{\psi}_L$ , thus the theory is applicable only to neutral fermions. Neutrinos are the only neutral elementary particles in the SM – the only possible Majorana particle candidate. This theory constructs a neutrino Majorana mass term  $\mathcal{L}_5$  of the following form in the Higgs unitary gauge

$$\mathcal{L}_5 = \frac{1}{2} \frac{gv^2}{\mathcal{M}} \nu_L^T \mathcal{C}^\dagger \nu_L, \quad (1.12)$$

where  $g$  is the coupling coefficient,  $v$  the Higgs VEV and  $\mathcal{M}$  a constant with the dimension of the mass proportional to the scale of new physics. The  $\mathcal{L}_5$  term would introduce a non-renormalizable term in the lagrangian, since it has dimensions of energy to the fifth power. This is not allowed in the SM term; however, the existence of such terms is plausible if we consider the SM an effective theory at low energy, manifestation of the symmetry breaking of a Grand Unified Theory (GUT) at higher energy, and not the definitive theory. The mass term in eq 1.12 implies the neutrino mass to be  $m = \frac{gv^2}{\mathcal{M}}$ . The coupling coefficient can be of the order of any other fermion's coupling coefficient, since the smallness of neutrino masses is achieved by the big value of the new physics mass scale alone. This vanilla formulation is the conceptual basis for many flavors of GUT-based *seesaw mechanism* [40], which we will not discuss here in any detail. However, it is fascinating how the puzzle of the neutrino mass hints to the existence of a deeper and more complete theory.

From a kinematic point of view, Dirac and Majorana neutrinos satisfy the same energy-momentum dispersion relationship. Thus, it is impossible to discern the neutrino nature through kinematic effects such as neutrino oscillations. Neutrinoless double beta decay searches are the most promising way to understand the nature of the neutrino and are therefore subject of great theoretical and experimental interest.

Observation of the lepton number violating process  $0\nu\beta\beta$  would imply neutrinos have a Majorana component. Depending on the mass hierarchy, the theory also predicts  $0\nu\beta\beta$  exclusion regions and confirmation of the sole Dirac component for neutrinos [find CIT](#).

Critical challenges await the next decade of experimental neutrino physics. Following the recommendation of the latest Particle Physics Project Prioritization Panel [36], the US is dedicating substantial resources to the development of a short- and long- baseline neutrino program to address many of these fundamental questions. This program pivots on the Liquid Argon Time Projection Chamber (LArTPC) detector technology which will be described in 2.

The main goals of these research programs include:

- Assessment of the existence of right-handed sterile neutrinos.
- Determination of the sign of  $\Delta m_{13}^2$  (or  $\Delta m_{23}^2$ ), i.e., the neutrino mass hierarchy.
- Determination of the octant, i.e. whether  $\theta_{23}$  is maximal.
- Determination the status of CP symmetry in the lepton sector.

### 1.3.2 Towards a more fundamental theory: GUTs

Despite its highly predictive power, a number of conceptual issues arise in the SM which disfavor it to be a good candidate for a fundamental theory.

The SM rather complex group structure, where a gauge group is formed with the direct product of other three groups as shown in eq. 1.1, is unexplained. Also, the SM fails to include a suitable dark matter candidate and a mechanisms that accounts for the baryon asymmetry of the universe. Within the SM, a total of 25 parameters remain seemingly arbitrary and need to be fitted to data: 3 gauge couplings, 9 charged

fermion masses, 3 mixing angles and one CP phase in the CKM matrix, the Higgs mass and quartic coupling,  $\theta_{QCD}$ , 3 neutrino masses, 3 neutrino mixing angles, 1 Dirac phase and, eventually, 2 Majorana phases.

## Nucleon decay

Baryon number is accidentally conserved in the Standard Model. Even though no baryon number violation has been experimentally observed thus far, no underlying symmetry in line with the Noether paradigm [32] explains its conservation. Almost all Grand Unified Theories predict at some level baryon number violation in the form of nucleon decay on long time-scales. Given the impossibility to reach grand unification energy scales with collider experiments ( $\sqrt{s} > 10^{15}$  GeV), an indirect proof of GUT is needed. The experimental observation of nucleon decay may be the only viable way to explore these theories and it is therefore a subject of great interest [?].

## 1.4 Motivations for Hadronic Cross Sections in Argon

### 1.4.1 Pion-Argon Total Hadronic Cross Section

This section outlines the importance of the pion-argon total hadronic cross section. We start by discussing the measurement in the context of neutrino interaction searches and of light mesons interaction with nuclei studies. We then describe the signal signature and historical measurements of pion-nucleus cross section, as well as the implementation of this cross sections in the current version of the simulation package used by LArIAT.

## **$\pi^-$ Ar Cross section in the Context of Neutrino Searches**

### **$\pi^-$ Ar Cross Section in the Context of Light Mesons Interaction with Nuclei Signal Signatures**

#### **Previous measurements: Lighter and Heavier Nuclei**

#### **Pion Interaction Cross Section for thin target in Geant4**

### **1.4.2 Kaon-Argon Total Hadronic Cross Section**

This section outlines the importance of the kaon-argon total hadronic cross section. We start by discussing the measurement in the context of nucleon decay searches and of light mesons interaction with nuclei studies. We then describe the signal signature and historical measurements of kaon-nucleus cross section, as well as the implementation of this cross sections in the current version of the simulation package used by LArIAT.

## **$K^+$ Ar Cross section in the Context of Nucleon Decay Searches**

In case of nucleon decay discovery, the dominant decay mode may uncover additional information about the GUT type. Supersymmetric GUTs [7,13] prefer the presence of kaons in the products of the decay, e.g.  $p \rightarrow K^+ \bar{\nu}$  (see fig 1.1, left). Gauge mediated GUTs, in which new gauge bosons are introduced that allow for the transformation of quarks into leptons, and vice versa, prefer the mode  $p \rightarrow e^+ \pi^0$  (see fig 1.1, right).

LArIAT tiny active volume makes it impossible for the experiment to place competitive limits on nucleon decay searches. However, LArIAT provides excellent data to characterize kaons in liquid argon for the “LAr golden mode”,  $p \rightarrow K^+ \bar{\nu}$ . The result of these studies will affect future proton decay searches in LArTPCs. Previous work has been done to assess the potential identification efficiency for different decay modes in a LArTPC [16], but, as the time of this writing, no study of kaon selection

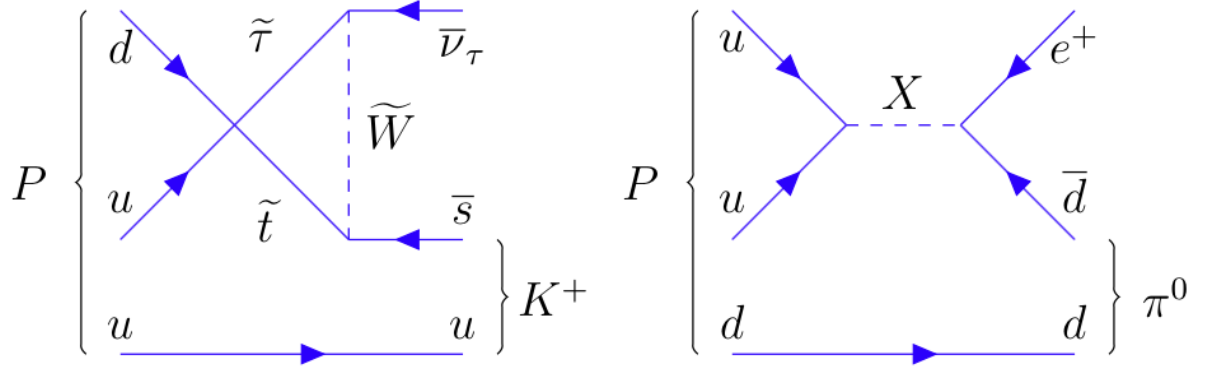


Figure 1.1: Feynman diagrams for proton decay “golden modes”:  $p \rightarrow K^+\bar{\nu}$  for supersymmetric GUTs on the left and  $p \rightarrow e^+\pi^0$  for gauge-mediated GUTs on the right.

efficiency in LArTPCs has been performed on data. The  $K^+$ -Ar interaction cross section has never been measured before and can affect the possibility of detecting and measuring kaons when produced in a proton decay event. Kaon interactions with argon can distort the kaon energy spectrum as well as change the topology of single kaon events. In a LArTPC, non-interacting kaons appear as straight tracks with a high ionization depositions at the end (Bragg peak). The topology of interacting kaons can be quite different. In case of elastic scattering, a distinct kink will be present in the track. In case of inelastic scattering the Bragg peak will not be present and additional tracks will populate the event. Performing the total hadronic  $K^+$ -Ar cross section measurement on data serves the double purpose of identifying the rate of “unusual” topologies (kinks and additional tracks) and of developing tools for kaon tracking in LAr.

### **$K^+$ Ar Cross section in the Context of Light Mesons Interaction with Nuclei**

The intrinsic value of the total hadronic  $K^+$ -Ar cross section measurement is that kaon interactions complement the measurements of  $\pi$  interactions as a probe of hadron interaction inside the nucleus in the strange sector. **High theoretical interest in probing**

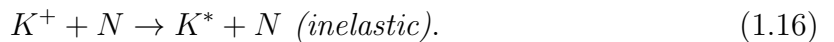
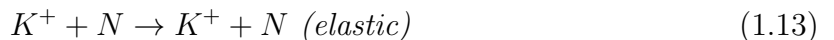
## constituent quark model of nuclear structure with KAON-NUCLEON INTERACTIONS CHIEDI REFERENZE A FLAVIO

### Signal Signatures

The interaction of a mildly relativistic charged kaon with an argon nucleus is determined largely by the strong force. The total hadronic  $K^+$ -Ar interaction cross section is defined as the one related to the single (hadronic) process driven only by the strong interaction. In this case, “total” indicates all strong interactions regardless of the final state. This condition purposefully includes both elastic and inelastic (reaction) channels. Indeed, the total cross section section can be then decomposed into

$$\sigma_{Tot} = \sigma_{Elastic} + \sigma_{Reaction}.$$

For the LArIAT cross section analysis, the kaons considered span a momentum inside the TPC from 800 MeV/c and 100 MeV/c. In this energy range, the relevant K-Nucleon interactions are according to [21]:



### Previous Measurements: Lighter and Heavier Nuclei

In general, measurements on kaon cross sections are extremely scarce. The measurement of the kaon interaction cross section would bring the additional benefit of reducing the uncertainties associated with hadron interaction models adopted in

MC simulations for argon targets, beneficial for both proton decay studies and kaon production from neutrino interaction studies, where the uncertainties for final state interaction models are big [14].

Figure 1.2 shows a 1997 measurement on several elements as performed by Friedmann et al. [23]. As a reference, this paper measures a  $\sigma_{Tot}$  for Si of  $366.5 \pm 4.8$  mb and a  $\sigma_{Tot}$  for Ca of  $494.6 \pm 7.7$  mb at 488 MeV/c. The cross section for argon is expected to lie in between these two measurements. Additional data on the kaon cross section are provided by Bugg et al. [9]. Bugg performs a measurement of the total  $K^+$  and  $K^-$  cross sections on protons and deuterons over the range of 0.6-2.65 GeV/c, as well as a measurement of the total  $K^+$  and  $K^-$  cross sections on carbon for a number of momenta; the results of this paper on carbon are reported in Figure 1.3.

### **Kaon Interaction Cross Section for thin target in Geant4**

Since the kaon cross section in argon has never been measured before, simulation packages tune kaon transportation in argon by extrapolation from lighter and heavier nuclei. LArIAT uses the Geant4 suite for particle transportation. Since kaon data on carbon are available, we used it as a metric to evaluate the Geant4 prediction performances. Figure 1.4 shows the total hadronic cross section for carbon implemented in Geant4 10.01.p3 overlaid with the Bugg and Friedman data. Unfortunately, the current version of Geant4 does not reproduce the data for carbon closely. On one hand, this evidence makes us even more wary when using the Monte Carlo in simulating the kaon-argon interactions. On the other, it further highlights the importance of the kaon measurement.

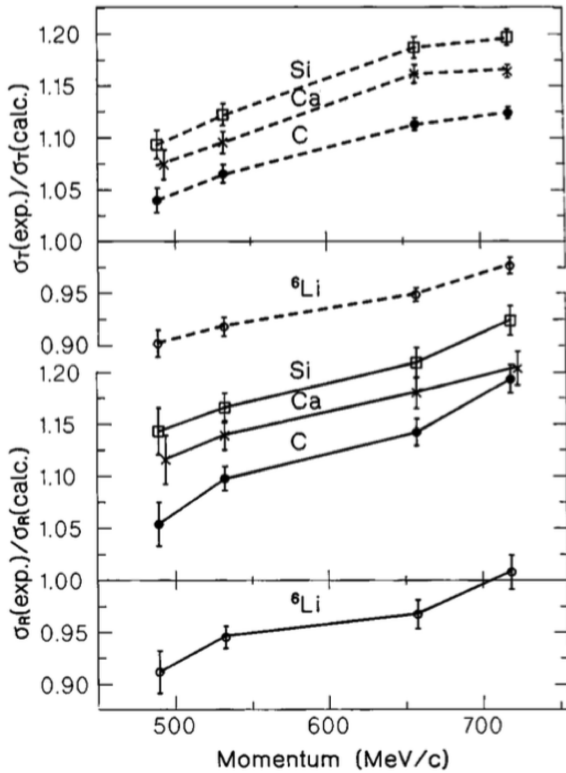


Figure 1.2: Ratios between experimental and calculated cross sections as from [23].  
Top: Total cross sections.  
Bottom: reaction cross sections.

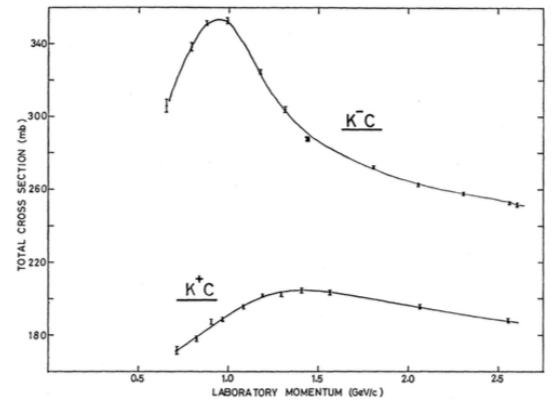


Figure 1.3: Total  $K^+$  and  $K^-$  cross sections on carbon as from [9].

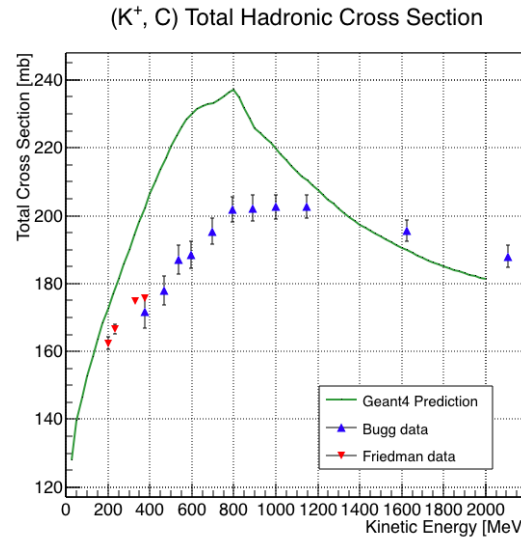


Figure 1.4: total hadronic cross section for carbon implemented in Geant4 10.01.p3 with overlaid with the Bugg and Frideman data.

## Chapter 2

# Liquid Argon Detectors at the Intensity Frontier

In the next few years, LArTPC experiments – such as the Short-Baseline Neutrino program (SBN) and DUNE – will be major players in the intensity frontier field.

## 2.1 Liquid Argon Time Projection Chambers at the Intensity Frontier

### 2.1.1 Time Projection Chamber

### 2.1.2 Ionization Detectors with Noble Liquids

### 2.1.3 LArTPC: Principles of Operation

#### 2.1.4 Liquid Argon Ionization Charge Detection

Electron Life Time & purity

Space Charge Effect

Recombination Effect

### 2.1.5 Liquid Argon scintillation Light Detection

LAr Scintillation Process

Wavelength Shifting of LAr Scintillation Light

## 2.2 The SBN Program: Neutrino Interaction and Detection

## 2.3 DUNE: Rare Decay Searches

The key elements for a rare decay experiment are: massive active volume, long exposure, high identification efficiency and low background. Figure 2.1 shows the current best experimental limits on nucleon decay lifetime over branching ratio (dots). Historically, the dominant technology used in these searches has been water Cherenkov de-

tectors: all the best experimental limits on every decay mode are indeed set by Super-Kamiokande [?, ?]. It is particularly important to notice that the kaon energy for the proton decay mode  $p \rightarrow K^+ \bar{\nu}$  is under Cherenkov threshold. Super-Kamiokande set the limit on the lifetime for the  $p \rightarrow K^+ \bar{\nu}$  mode by relying exclusively on photons from nuclear de-excitation. For this reason, an attractive alternative approach to identifying nucleon decay is the use of a Liquid Argon Time Projection Chamber (LArTPC).

LArTPCs can complement nucleon decay searches in modes where water Cherenkov detectors are less sensitive, especially  $p \rightarrow K^+ \bar{\nu}$ . According to [?], DUNE will have an active volume large enough, have sufficient shielding from the surface, and will run for lengths of time sufficient to compete with Hyper-K, opening up the opportunity for the discovery of nucleon decay.

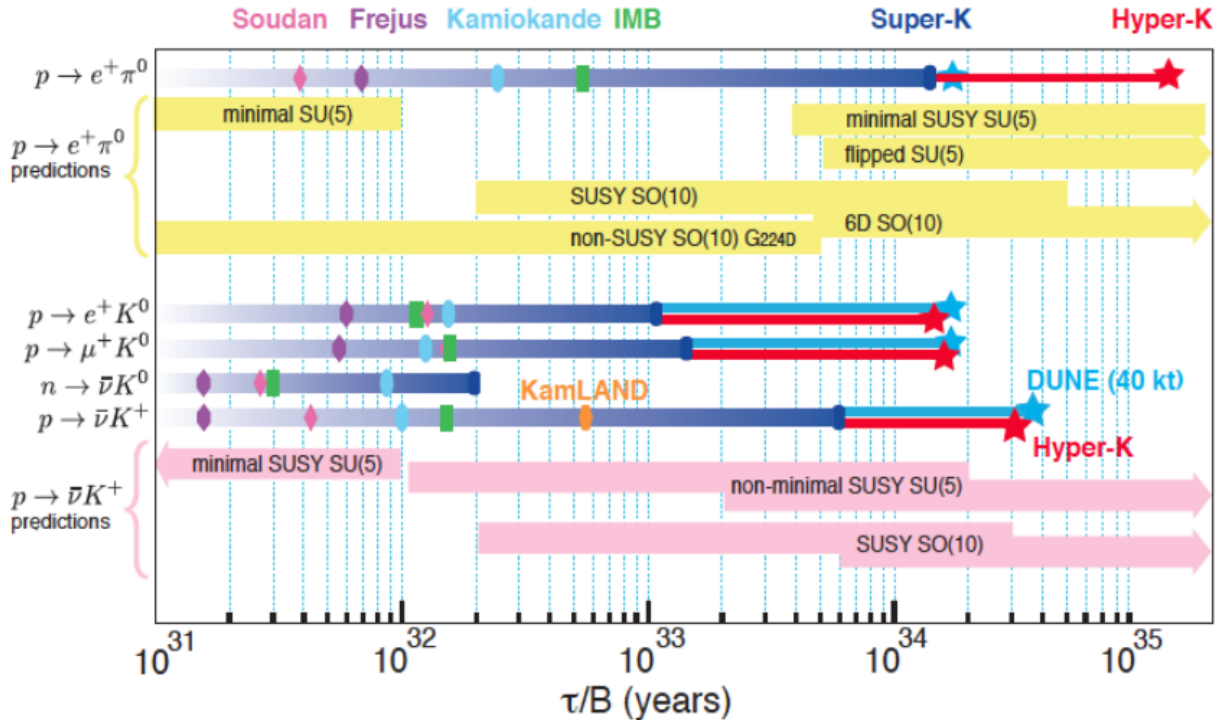


Figure 2.1: Proton decay lifetime limits from passed and future experiments.

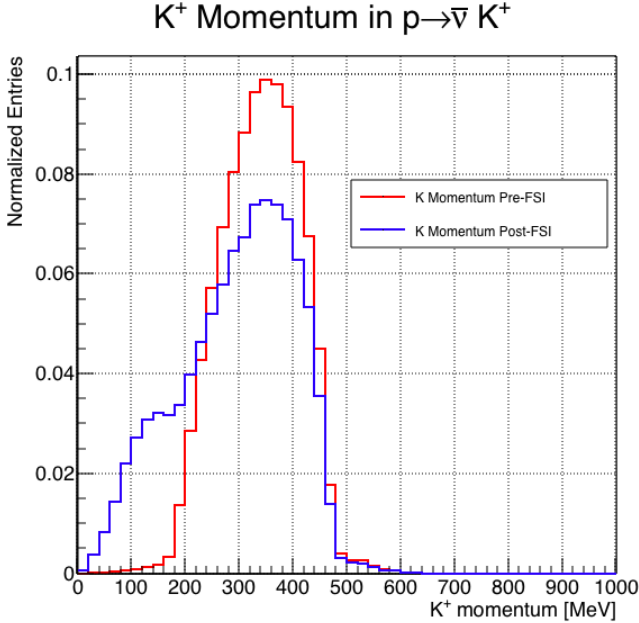


Figure 2.2: Momentum of the kaon outgoing a proton decay event as simulated by the Genie 2.8.10 event generator in argon. The red line represent the kaon momentum distribution before undergoing the simulated final state interaction inside the argon nucleus, while the blue line represents the momentum distribution after FSI.

## 2.4 Enabling the next generation of discoveries: LArIAT

LArIAT, a small Liquid Argon Time Projection Chamber (LArTPC) in a test beam, is designed to perform an extensive physics campaign centered on charged particle cross section measurements while characterizing the detector performance for future LArTPCs. LArTPC represents one of the most advanced experimental technologies for physics at the Intensity Frontier due to its full 3D-imaging, excellent particle identification and precise calorimetric energy reconstruction. This complex technology however needs a thorough calibration and dedicated measurements of some key quantities to achieve the precision required for the next generation of discoveries at the Intensity Frontier which LArIAT can provide.

The LArIAT LArTPC is deployed in a dedicated calibration test beamline at Fer-

milab. We use the LArIAT beamline to characterize the charge particles before they enter the TPC: the particle type and initial momentum is known from beamline information. The precise calorimetric energy reconstruction of the LArTPC technology enables the measurement of the total differential cross section for tagged hadrons. The Pion-Nucleus and Kaon-Nucleus total hadronic interaction cross section have never been measured before in argon and they are a fundamental step to shed light on light meson interaction in nuclei. Additionally, these measures provides a key input to neutrino physics and proton decay studies in future LArTPC experiments like SBN and DUNE. **add paragraph on all wonderful things lariat can do... some event displays would be nice!**

**ADD genie proton decay kaon distribution and lariat beamline overlayed** The signature of a proton decay event in the “LAr golden mode” is the presence of a single kaon of about 400 MeV in the detector.

# Chapter 3

## LArIAT: Liquid Argon In A Testbeam

In this chapter, we describe the LArIAT experimental setup. We start by illustrating the journey of the charge particles in the Fermilab accelerator complex, from the gaseous thermal hydrogen at the Fermilab ion source to the delivery of the LArIAT tertiary beam at MC7. We then describe the LArIAT beamline detectors, the LArTPC, the DAQ and the monitoring system.

### 3.1 The Particles Path to LArIAT

LArIAT's particles history begins in the Fermilab accelerator complex with a beam of protons. The process of protons acceleration develops in gradual stages (see picture 3.1): gaseous hydrogen is ionized in order to form  $H^-$  ions; these ions are boosted to 750 keV by a Cockcroft-Walton accelerator and injected to the Linac linear accelerator that increases their energy up to 400 MeV; then,  $H^-$  ions pass through a carbon foil and lose the two electrons; the resulting protons are then injected into a rapid cycling synchrotron, called Booster; at this stage, protons reach 8 GeV of energy and are compacted into bunches; the next stage of acceleration is the Main Injector,

a synchrotron which accelerates the bunches up to 120 GeV; in the Main Injector, several bunches are merged into one and used for the injection in the last stage.

The Fermilab accelerator complex works in supercycles of roughly 60 seconds in duration. The beam is split by electrostatic septa and delivered at different experimental halls all over the lab. A 120 GeV/c primary proton beam with variable intensity is extracted in four-second “spills” and sent to the Meson Center beam line.

LArIAT’s home at Fermilab is the Fermilab Test Beam Facility (FTBF), where the experiment characterizes a beam of charge particles downstream from the Meson Center beam line. Here, the primary beam is focused onto a tungsten target to create LArIAT’s secondary beam. The composition of the secondary particle beam is mainly positive pions. The momentum peak of the secondary beam was fixed at 64 GeV/c for the LArIAT data considered in this work, although the beam is tunable in momentum between 8-80 GeV/c; this configuration of the secondary beamline assured a stable beam delivery at the LArIAT experimental hall.

The secondary beam impinges then on a copper target within a steel collimator inside the LArIAT experimental hall (MC7) to create the LArIAT tertiary beam, (shown in Fig. 3.2). The steel collimator selects particles produced with a 13° production angle at the target down the beamline. The particles are then bent by 10° through a pair of dipole magnets. By configuring the field intensity of the magnets we allow the particles of LArIAT’s tertiary beam to span a momentum range from 0.2 to 1.4 GeV/c. The polarity of the magnet is also configurable and determines the sign of the beamline particles which are focused on the LArTPC. If the magnets polarity is positive the tertiary beam composition counts mostly pions and protons with a small fraction of electrons, muons, and kaons. It is the job of the LArIAT beamline detectors to select the particles polarity, to perform particle identification in the beamline and to measure the momentum of the tertiary beam particles before they get to the LArTPC. The LArIAT detectors are described in the following paragraphs.

## Fermilab Accelerator Complex

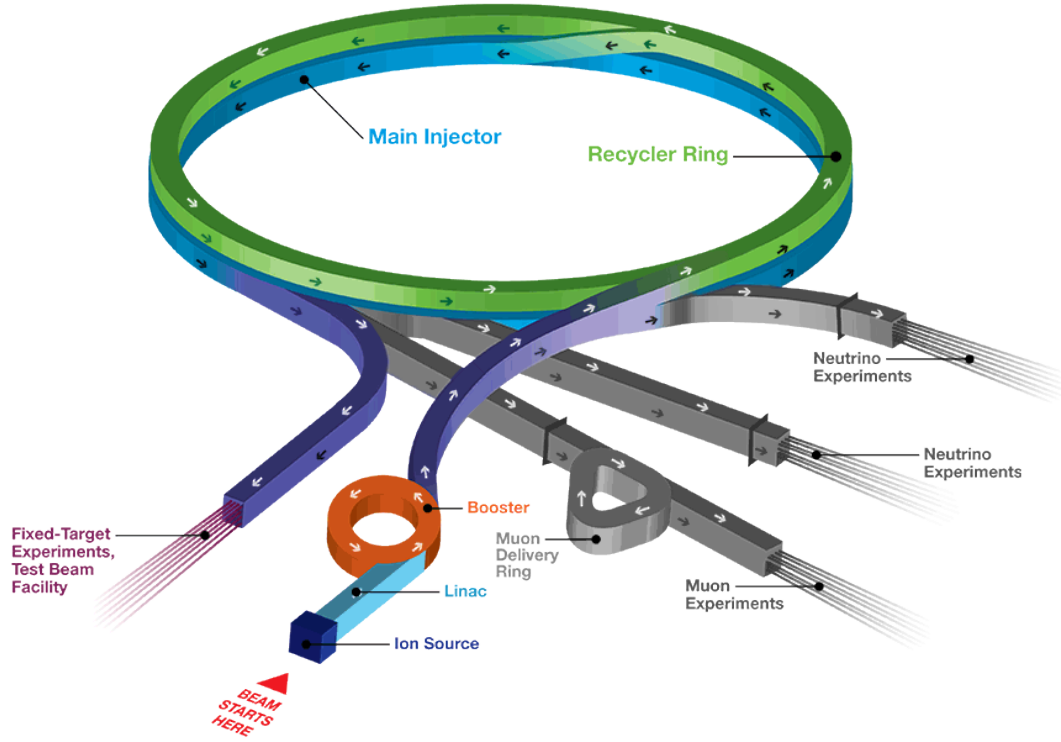


Figure 3.1: Layout of Fermilab Acellerator complex.

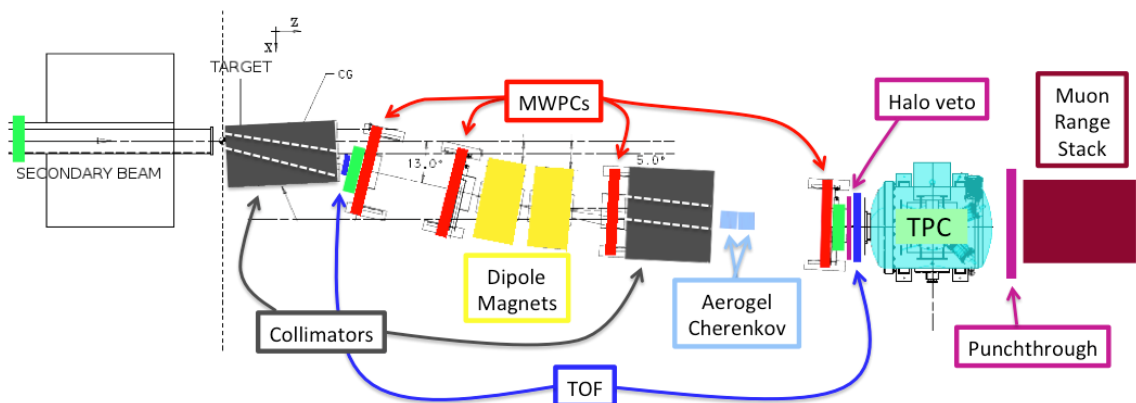


Figure 3.2: Bird's eye view of the LArIAT tertiary beamline. In grey: upstream and downstream collimators; in yellow: bending magnets; in red: wire chambers; in blue: time of flight; in green: liquid argon TPC volume; in maroon: muon range stack.

## 3.2 LArIAT Tertiary Beam Instrumentation

The instrumentation of LArIAT tertiary beam and the TPC components have changed several times during the three years of LArIAT data taking. The following paragraphs describe the components operational during “Run II”, the data taking period relevant to the hadron cross section measurements.

The key components of the tertiary beamline instrumentation for the hadron cross section analyses are the two bending magnets, a set of four wire chambers (WCs) and two time-of-flight scintillating paddles (TOF) and, of course, the LArTPC. The magnets determine the polarity of the particles in the tertiary beam; the combination of magnets and wire chambers determines the particles’ momentum, which is used to determine the particle species in conjunction with the TOF. A muon range stack downstream from the TPC and two sets of cosmic paddles configured as a telescope surrounding the TPC are also used for calibration purposes.

### 3.2.1 Bending Magnets

LArIAT uses a pair of identical Fermilab type “NDB” electromagnets, recycled from the Tevatron’s anti-proton ring, in a similar configuration used for the MINERvA T-977 test beam calibration [18]). The magnets are a fundamental piece of the LArIAT beamline equipment, as they are used for both particle identification and momentum measurement before the LArTPC. The sign of the current in the magnets allows us to select either positively or negatively charged particles; the value of the magnetic field is used in the momentum determination and in the subsequent particle identification.

We describe here the characteristics and response of one magnet, as the second one has a similar response, given its identical shape and history. Each magnet is a box with a rectangular aperture gap in the center to allow for the particle passage. The magnet aperture measures 14.224 cm in height, 31.75 cm in width, and 46.67 cm in length.

Since the wire chambers aperture ( $\sim 12.8 \text{ cm}^2$ ) is smaller than the magnet aperture, only the central part of the magnet gap is utilized. The field is extremely uniform over this limited aperture and was measured with two hall probes, both calibrated with nuclear magnetic resonance probes. The probes measured the excitation curve shown in Figure 3.3.

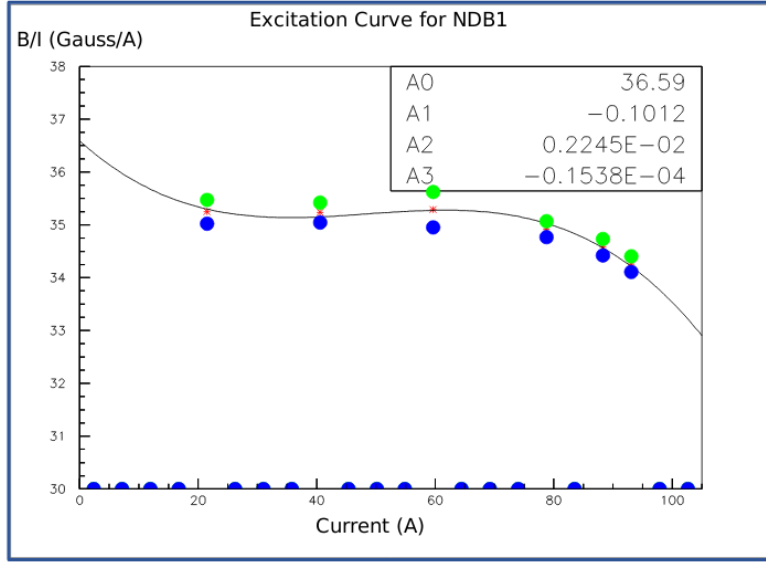


Figure 3.3: Magnetic field over current as a function of the current, for one NDB magnet (excitation curve). The data was collected using two hall probes (blue and green). We fit the readings with a cubic function (black) to average of measurements (red) given in the legend.

The current through the magnets at a given time is identical in both magnets. For the Run II data taking period, the current settings explored were 60A ( $B \sim 0.21 \text{ T}$ ) and 100A ( $B \sim 0.35 \text{ T}$ ) in both polarities. Albeit advantageous to enrich the tertiary beam composition with high mass particles such as kaons, we never pushed the magnets current over 100 A, not to incur in overheating. During operation, we operated a air and water cooling system on the magnets and we remotely monitored the magnets temperature.



Figure 3.4: One of the four Multi Wire Proportional Chambers (WC) used in the LArIAT tertiary beamline and relative read-out electronics.

### 3.2.2 Multi-Wire Proportional Chambers

LArIAT uses four multi-wire proportional chambers, or wire chambers (WC) for short, two upstream and two downstream from the bending magnets. The geometry of one chamber is shown in Figure 3.4: the WC effective aperture is a square of 12.8 cm perpendicular to the beam direction. Inside the chamber, the 128 horizontal and 128 vertical wires hang at a distance of 1 mm from each other in a mixture of 85% Argon and 15% isobutane gas. The WC operating voltage is between 2400 V and 2500 V. The LArIAT wire chambers are an upgraded version of the Fenker Chambers [20], where an extra grounding improves the signal to noise ratio of the electronic readout.

Two ASDQ chips [31] mounted on a mother board plugged into the chamber serve as front end amplifier/discriminator. The chips are connected to a multi-hit TDC [26] which provides a fast OR output used as first level trigger. The TDC time resolution is 1.18 ns/bin and can accept 2 edges per 9 ns. The maximum event rate acceptable by the chamber system is of 1 MHz: this rate is not a limiting factor considering that **the rate of the tertiary particle beam at the first wire chamber is estimated to be less than 15 kHz**. A full spill of data occurring once per supercycle is stored on the TDC board memory at once and read out by a specially designed controller. We use LVDS cables to carry both power and data between the controller and the TDCs and from

the controller to the rest of the DAQ.

### Multi-Wire Proportional Chambers functionality

We use the wire chamber system together with the bending magnets to measure the particle's momentum.

In the simplest scenario, only one hit on each and every of the four wire chambers is recorded during a single readout of the detector systems. Thus, we use the hit positions in the two wire chambers upstream of the magnets to form a trajectory before the bend, and the hit positions in the two wire chambers downstream of the magnets to form a trajectory after the bend. We use the angles in the XZ plane between the upstream and downstream trajectories to calculate the  $Z$  component of the momentum as follows:

$$P_z = \frac{B_{eff}L_{eff}}{3.3(\sin(\theta_{DS}) - \sin(\theta_{US}))}, \quad (3.1)$$

where  $B_{eff}$  is the effective maximum field in a square field approximation,  $L_{eff}$  is the effective length of both magnets (twice the effective length of one magnet),  $\theta_{US}$  is the angle off the  $z$  axis of the upstream trajectory,  $\theta_{DS}$  is the angle off the  $z$  axis of the downstream trajectory and  $3.3 c^{-1}$  is the conversion factor from [T·m] to [MeV/c]. By using the hit positions on the third and fourth wire chamber, we estimate the azimuthal and polar angles of the particle trajectory, and we are able to calculate the other components of the momentum.

The presence of multiple hits in a single wire chamber or the absence of hits in one (or more) wire chambers can complicate this simple scenario. The first complication is due to beam pile up, while the latter is due to wire chamber inefficiency. In the case of multiple hits on a single WC, at most one wire chamber track is reconstructed per event. Since the magnets bend particles only in the X direction, we assume the particle trajectory to be roughly constant in the YZ plane, thus we keep the

combination of hits which fit best with a straight line. It is still possible to reconstruct the particle’s momentum even if the information is missing in either of the two middle wire chambers (WC2 or WC3), by constraining the particle trajectory to cross the plane in between the magnets.

Events satisfying the simplest scenario of one single hit in each of the four wire chambers form the “Picky Track” sample. We construct another, higher statistics sample, where we loosen the requirements on single hit and wire chamber efficiency: the “High Yield” sample. For LArIAT Run II, the High Yield sample is about three times the Picky Tracks statistics. For the first measurements of the LArIAT hadronic cross section, we use the Picky Tracks sample because the uncertainty on the momentum is smaller and the comparison with the beamline MC results is straightforward compared with the High Yield sample; a possible future update and cross check of these analysis would be the use of the High Yield sample.

#### Four point track momentum uncertainty

### 3.2.3 Time-of-Flight System

Two scintillator paddles, one upstream to the first set of WCs and one downstream to the second set of WCs form LArIAT time-of-flight (TOF) detector system.

The upstream paddle is made of a 10 x 6 x 1 cm scintillator piece, read out by two PMTs mounted on the beam left side which collect the light from light guides mounted on all four edges of the scintillator. The downstream paddle is a 14 x 14 x 1 cm scintillator piece read out by two PMTs on the opposite ends of the scintillator. The relatively thin width on the beamline direction minimizes energy loss of the particles coming from the target in the scintillator material.

The CAEN 1751 digitizer is used to digitize the TOF PMTs signals at a sampling rate of 1 GHz. The 12 bit samples are stored in a circular memory buffer. At trigger time, data from the TOF PMTs are recorded to output in a 28.7  $\mu$ s windows starting

approximately 8.4  $\mu$ s before the trigger time.

### TOF functionality

The TOF signals rise time (10-90%) is 4 ns and a full width, half-maximum of 9 ns consistent in time. The signal amplitudes from the upstream TOF and downstream TOF are slightly different: 200 mV for the upstream PMTs but only 50 mV for downstream PMTs. The time of the pulses was calculated utilizing an oversampled template derived from the data itself. We take the pulse pedestal from samples far from the pulse and subtract it to the pulse amplitude. We then stretch vertically a template to match the pedestal-subtracted pulse amplitude and we move it horizontally to find the time. With this technique, we find a pulse time-pickoff resolution better than 100 ps. The pulse pile up is not a significant problem given the TOF timing resolution and the rate of the particle beam. Leveraging on the pulses width uniformity of any given PMT, we flag events where two pulses overlap as closely in time as 4 ns with an 90% efficiency according to simulation.

We combine the pulses from the two PMTs on each paddle to determine the particles' arrival time by averaging the time measured from the single PMT, so to minimize errors due to optical path differences in the scintillator. However, a time spread of approximately 300 ps is present in both the upstream and downstream detectors, likely due to transit time jitter in the PMTs themselves. There is no evidence of systematic timing drift over long data-taking periods such as 3-4 months: the maximum variation of the average time differences between pairs of PMTs reading out the same scintillator is of the order of 150 ps.

### 3.2.4 Punch-Through and Muon Range Stack Instruments

The punch-thorough and the muon range stack (MuRS) detectors are located downstream of the TPC. These detectors provide a sample of TPC crossing tracks without



Figure 3.5: Image of the down stream time of flight paddle, PMTs and relative support structure before mounting.

relying on TPC information and can be used to improve particle ID for muons and pions with momentum higher than 450 MeV/c.

The punch-thorough is simple sheet of scintillator material, read out by two PMTs. The MuRS is a segmented block of steel with four slots instrumented with scintillation bars. The four steel layers in front of each instrumented slot are 2 cm, 2 cm, 14 cm and 16 cm wide in the beam direction. Each instrumented slot is equipped with four scintillation bars each, positioned horizontally in the direction orthogonal to the beam. Each scintillator bar measures  $\text{?} \times \text{?} \times 2$  cm and it is read out by one PMT.

The signals from both the punch-thorough and the MuRS PMTs are digitized in the CAEN V1740, same as the TPC; the details of this discriminator are laid out in 3.3.2. It is worth noticing that the sampling time of the CAEN V1740 is slow (of the order of 128 ns), so pulse shape information from the PMT is lost. Punch-thorough and MuRS hits are formed utilizing the digital discriminator signals under threshold at a given time, where we obtain the threshold for each PMT directly on data distributions.

### 3.2.5 LArIAT Cosmic Ray Paddle Detectors

LArIAT triggers both on beam events and on cosmic rays events. We perform this latter trigger by using two sets of cosmic ray paddle detectors (a.k.a. “cosmic towers”.) The cosmic towers frame the LArIAT cryostat, as one sits in the downstream left corner and the other sits in the upstream right corner of the cryostat. Two paddle sets of four scintillators pieces each make up each cosmic tower, an upper set and a lower set per tower. Of the four paddles, a couple of two matched paddles stands upright while the a second matched pair lies across the top of the assembly in the top sets (or across the bottom of the assembly in the bottom sets). The horizontal couple is used as a veto for particles traveling from inside the TPC out. The four signals from the vertical paddles along one of the body diagonals of the TPC are combined in a logical “AND”. This allows to select cosmic muons crossing the TPC along one of its diagonals. Cosmic ray tracks crossing both anode and cathode populate the events triggered this way. This particularly useful sample of tracks (which we can safely assume to be associated with 5 GeV muons) can be used for many tasks; for example, we use anode-cathode piercing tracks to cross check the TPC electric field on data (see Appendix A), to calibrate the charge response of the TPC wires for the full TPC volume and to measure the electron lifetime in the chamber (see section 5.3).

A Zener-diode Hamamatsu H5783 PMT collects the light from a wavelength-shifting optical fiber which runs along one of the long sides of each paddle. A custom-made PMT Amplifier and Discrimination (PAD) circuit mounted at one end of the paddle collects signals from the PMTs and sends them to the Control and Concentrator Unit (CCU). We use the same connection to power the PMT, control voltage and threshold, and output the PMT signal as logic ECL pulse. We retrieved the scintillation paddles from the decommissioning of the CDF detector at Fermilab and we used only the paddles with a counting efficiency greater than 95% and low noise at working

voltage. The measured trigger rate of the whole system is 0.032 Hz, corresponding to  $\sim 2$  muons per minute.



Figure 3.6: Photograph of one of the scintillation counters used in the cosmic towers.

### 3.3 In the Cryostat

#### 3.3.1 Cryogenics and Argon Purity

LArIAT repurposed the ArgoNeuT cryostat [5] in order to use it in a beam of charge particles, and added a new process piping and a new liquid argon filtration system in FTBF. Inside the LArIAT experimental hall, the cryostat sits on the beam of charge particles with its horizontal main axis oriented parallel to the beam.

Two volumes make up LArIAT cryostat, shown in Figure 3.7: the inner vessel and the outer vessel. Purified liquid argon fills the inner vessel, while the outer volume provides insulation through a vacuum jacket equipped with layers of aluminized mylar superinsulation. The inner vessel is a cylinder of 130 cm length and 6.2 cm diameter, containing about 550 L of LAr, corresponding to a mass of 0.76 ton. We run the signal cables for the LArTPC and the high voltage feedthrough through a “chimney” at the top and mid-length of the cryostat.

Given the different scopes of the ArgoNeuT and LArIAT detectors, we made

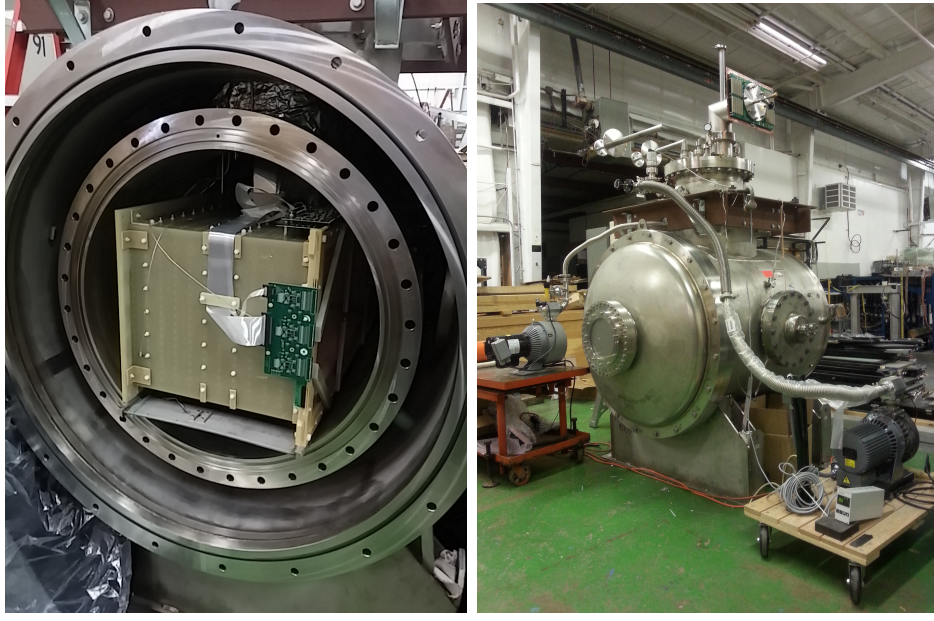


Figure 3.7: Left: the LArIAT TPC in the inner volume of the open cryostat. Right: cryostat fully sealed ready to be transported to FTBF.

several modification to the ArgoNeuT cryostat in order to use it in LArIAT. In particular, the modification shown in Figure 3.8 were necessary to account for the beam of charged particles entering the TPC and to employ the new FTBT liquid argon purification system. We added a “beam window” on the front outer end cap and an “excluder” on the inner endcap, with the scope of minimizing the amount of dead material upstream of the TPC’s active volume. Doing so, we reduced the amount of uninstrumented material before the TPC from  $\sim 1.6$  radiation lengths ( $X_0$ ) (ArgoNeuT) to less than  $0.3 X_0$  (LArIAT). To allow studies of the scintillation light, we added a side port feedthrough which enables the mounting of the light collection system, as well as the connections for the corresponding signal and high-voltage cables (see Section 3.3.3). We modified the bottom of the cryostat adding Conflat and ISO flange sealing to connect the liquid argon transfer line to the new argon cooling and purification system.

As in any other LArTPC, argon purity is a crucial parameter for LArIAT. Indeed, the presence of contaminants effects both the basic working principles of a



Figure 3.8: Main modifications to the ArgoNeuT cryostat: 1) outlet for connection to the purification system at the bottom of the cryostat; 2) the “beam-window” on the outer endcap and “excluder” which reduce the amount of non-instrumented material before the TPC; 3) the side port to host the light collection system.

LArTPC: electronegative contaminants such as oxygen and water decrease the number of ionization electrons collected on the wires after drifting through the volume, while contaminants such as Nitrogen decrease the light yield from scintillation light, especially in its slow component. In LArIAT, contaminations should not exceed the level of 100 parts per trillion (ppt). We achieve this level of purity in several stages. The specifics required for the commercial argon bought for LArIAT are 2 parts per million (ppm) oxygen, 3.5 ppm water, and 10 ppm nitrogen. This argon is monitored with the use of commercial gas analyzer. Argon is stored in a dewar external to LArIAT hall and filtered before filling the TPC. LArIAT uses a filtration system designed for the Liquid Argon Purity Demonstrator (LAPD) [19]: half of a 77 liter filter contains a 4A molecular sieve (Sigma-Aldrich [37]) apt to remove mainly water, while the other half contains BASF CU-0226 S, a highly dispersed copper oxide impregnated on a high surface area alumina, apt to remove mainly oxygen [8]. A single pass of argon in the filter is sufficient to achieve the necessary purity, unless the filter is saturated.

In case the filter saturates, the media needs to be regenerated by using heated gas; this happened twice during the Run II period<sup>1</sup>. The filtered argon reaches the inner vessel via a liquid feedthrough on the top of the cryostat. Argon is not recirculated in the system, rather it boils off and vent to the atmosphere. During data taking, we replenish the argon in the cryostat several times per day to keep the TPC high voltage feedthrough and cold electronics always submerged. In fact, we constantly monitor the level, temperature, and pressure of the argon both in the commercial dewar and inside the cryostat during data taking.

### 3.3.2 LArTPC: Charge Collection

The LArIAT Liquid Argon Time Projection Chamber is a rectangular box of dimensions 47 cm (width) x 40 cm (height) x 90 cm (length), containing 170 liters of Liquid Argon. The LArTPC three major subcomponents are

- 1) the cathode and field cage,
- 2) the wire planes,
- 3) the read-out electronics.

#### Cathode and field cage

A G10 plain sheet with copper metallization on one of the 40 x 90 cm inner surfaces forms the cathode. A high-voltage feedthrough on the top of the LArIAT cryostat delivers the high voltage to the cathode; scope of the high voltage system (Figure 3.9) is to drift ionization electrons from the interaction of charged particles in the liquid argon to the wire planes. The power supply used in this system is a Glassman LX125N16 [24] capable of generating up to -125 kV and 16 mA of current, but

---

1. We deemed the filter regeneration necessary every time the electron lifetime dropped under 100  $\mu$ s.

operated at -23.5kV during LArIAT Run-II. The power supply is connected via high voltage cables to a series of filter pots before finally reaching the cathode.

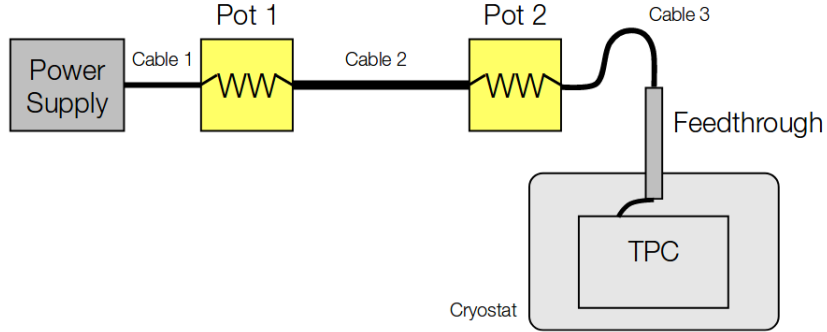


Figure 3.9: Schematic of the LArIAT high voltage system.

The field cage is made of twenty-three parallel copper rings framing the inner walls of the G10 TPC structure. A network of voltage-dividing resistors connected to the field cage rings steps down the high voltage from the cathode to form a uniform electric field. The electric field over the entire TPC drift volume is 486 V/cm (see A). The maximum drift length, i.e. the distance between cathode and anode planes, is 47 cm.

### Wire planes

The wire planes measure the charge deposited in the TPC active volume. The drifting charge induces a current on the wire of the inner planes and it is collected on the collection plane wires. LArIAT counts three wire planes separated by 4 mm spaces: in order of increasing distance from the cathode, they are the shield, the induction and the collection plane. The “wire pitch”, i.e., the distance between two consecutive wires in a given plane, is 4 mm. The shield plane counts 225 parallel wires of equal length oriented vertically. This plane is not connected with the read-out electronics; rather it shields the outer planes from extremely long induction signals due to the ionization chamber in the whole drift volume. As the shield plane acts almost like a

Faraday cage, the shape of signals in the first instrumented plane (induction) results easier to reconstruct. Both the induction and collection planes count 240 parallel wires of different length oriented at  $60^\circ$  from the vertical with opposite signs. Electrons moving past the induction plane will induce a bipolar pulse on its wires; the drifting electrons will be then collected on the collection plane's wires, forming a unipolar pulse.

The three wire planes and the cathode form three drift volumes, as shown in Figure 3.10. The main drift volume is defined as the region between the cathode plane and the shield plane (C-S). The other two drift regions are those between the shield plane and the induction plane (S-I), and between the induction plane and the collection plane (I-C). The electric field in these regions is chosen to satisfy the charge transparency condition and allow for 100% transmission of the drifting electrons through the shield and the induction planes.

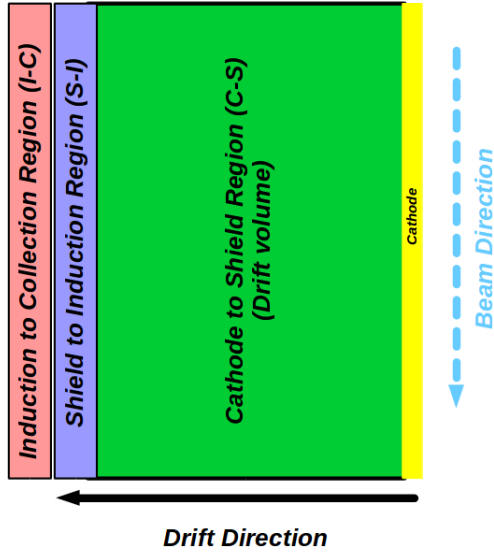


Figure 3.10: Schematic of the three drift regions inside the LArIAT TPC: the main drift volume between the cathode and the shield plane (C-S) in green, the region between the shield plane and the induction plane (S-I) in purple, and the region between the induction plane and the collection plane (I-C) in pink.

Table 3.1 provides the default voltages applied to the cathode and the shield,

induction, and collection plane.

Table 3.1: Cathode and anode planes default voltages

Cathode	Shield	Induction	Collection
-23.17 kV	-298.8 V	-18.5 V	338.5 V

## Electronics

Dedicated electronics read the induction and collection plane wires, for a total of 480-channel analog signal path from the TPC wires to the signal digitizers. A digital control system for the TPC-mounted electronics, a power supply, and a distribution system complete the front-end system. Figure 3.11 shows a block diagram of the overall system. The direct readout of the ionization electrons in liquid argon forms typically small signals on the wires, which need amplification in order to be processed. LArIAT performs the amplification stage directly in cold with amplifiers mounted on the TPC frame inside the liquid argon, achieving a remarkable Signal-to-Noise ratio. The signal from the ASICs are driven to the other end of the readout chain, to the CAEN V1740 digitizers. The CAEN V1740 has a 12 bit resolution and a maximum input range of 2 VDC, resulting in about 180 ADC count for a crossing MIP.

### 3.3.3 LArTPC: Light Collection System

The collection of scintillation photons is the second mechanism of particle detection in argon other than the ionization electrons. Over the course of LArIAT’s three years of data taking, the light collection system changed several times. We describe here the light collection system for Run II. Two PMTs, a 3-inch diameter Hamamatsu R-11065 and 2-inch diameter ETL D757KFL [2], as well as three SiPMs arrays (two Hamamatsu S11828-3344M 4x4 arrays and one single-channel SensL MicroFB-60035) are mounted on the PEEK support structure. PEEK screws into an access flange

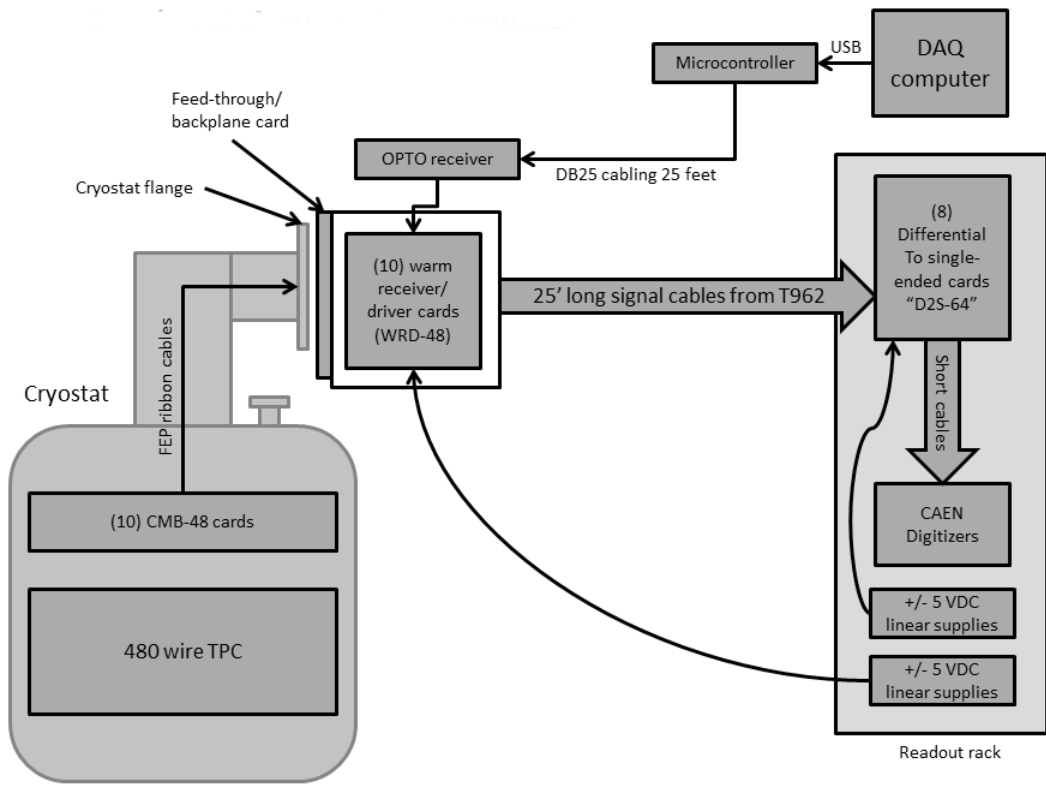


Figure 3.11: Overview of LArIAT Front End electronics.

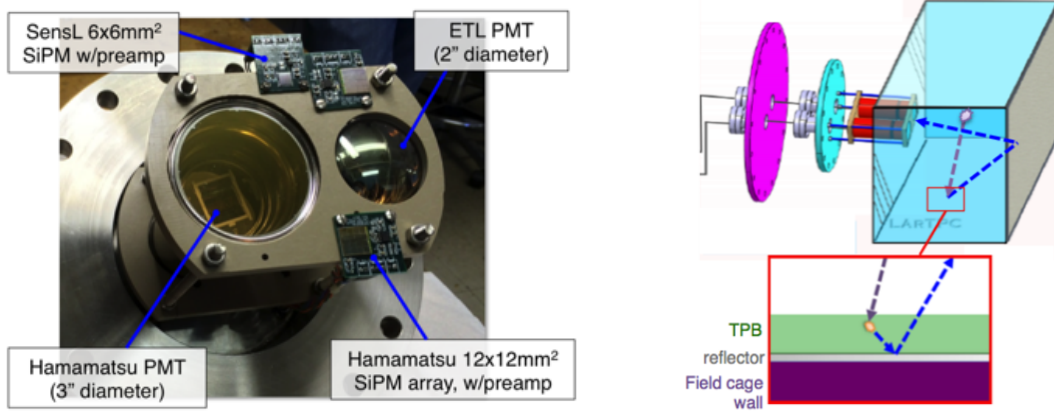


Figure 3.12: LArIAT’s photodetector system for observing LAr scintillation light inside the TPC (left), and a simplified schematic of VUV light being wavelength-shifting along the TPB-coated reflecting foils (right).

as shown in Figure 3.12, on the anode side, leaving approximately 5 cm of clearance from the collection plane.

Liquid argon scintillates in vacuum-ultraviolet (VUV) range at 128 nm; since cryogenic PMTs are not sensitive to VUV wavelengths, we need to shift the light in a region visible to the PMTs. In LArIAT, the wavelength shifting is achieved by installing on the four walls of the TPC highly-reflective VIKUITY dielectric substrate foils coated with a thin layer of tetraphenyl-butadiene (TPB). The scintillation light interaction with the TPC emits one or more visible photons, we are then reflected into the chamber. Thus, the light yield increases and results more uniform across the TPC active volume, allowing the possibility of light-based calorimetry, currently under study.

For Run II, we coated both the windows of the ETL PMT and SensL SiPM with a thin layer of TPB. In doing so, some of the VUV scintillation light converts into visible right at the sensor faces, keeping information on the direction of the light source. Information about the light directionality is lost for light reflected on foils, as the reflection is uniform in angle.

## 3.4 Trigger and DAQ

The LArIAT DAQ and trigger system governs the read out of all the many subsystems forming LArIAT. The CAEN V1495 module and its user-programmable FPGA are the core of this system. Every 10 ns, this module checks for matches between sixteen logical inputs and user-defined patterns in the trigger menu; if it finds a match for two consecutive clock ticks, that trigger fires.

LArIAT receives three logic from the Fermilab accelerator complex related to the beam timing which we use as input triggers: a pulse just before the beam, a pulse indicating beam-on, and a beam-off pulse.

The beam instruments, the cosmic ray taggers, and the light collection system provide the other NIM-standard logic pulse inputs to the trigger decision. We automatically log the trigger inputs configuration with the rest of the DAQ configuration at the beginning of each run.

Fundamental inputs to the trigger card come from the TOF (see Sec. 3.2.3) and the wire chambers (see Sec. 3.2.2), as activity in these systems points to the presence of a charged particle in tertiary beam line. In particular, the discriminated pulses from the TOF PMTs form a NIM logic pulse for the trigger logic. We ask for a coincidence within a 20 ns window for all the pulses from the PMTs looking at the same scintillator block and use the coincidence between the upstream and downstream paddle to inform the trigger decision. In order to form a coincidence between the upstream and downstream paddles, we delay the upstream paddle coincidence by 20 ns and widen it by 100 ns. The delay and widening are necessary to account for both lightspeed particles and slower particles (high-mass) to travel the 6.5 m between the upstream and the downstream paddles. For the read out of the wire chambers, we use a total of sixteen multi-hit TDCs, four per chamber: two TDC per plane (horizontal and vertical), sixty-four wires per TDC. In each TDC, we keep the logical “OR” for any signal over threshold from the sixty-four wires. We then require a

coincidence between the “OR” for the horizontal TDCs and the “OR” for the vertical TDCs: with this logic we make sure that at least one horizontal wire and one vertical wire saw significant signal in one wire chamber. The single logical pulse from each of the four wire chambers feeds into the first four inputs to the V1495 trigger card. We require a coincidence within 20 ns of at least three logical inputs to form a trigger.

The cosmic towers (see Section 3.2.5) provide another primary input to the trigger, in order to capture long tracks from cosmic muons crossing the TPC. We use NIM modules to require coincidences between one upper and one lower paddle set of any opposite cosmic towers. The OR all the opposite towers’ coincidences is fed as an input to the trigger card.

We use the signal from the cryogenic PMTs (see Section ??) to form several interesting triggers. The coincidence of signal from all the PMT pulses within  $\sim$ 20 ns is an indication of ionizing radiation in the TPC and forms a trigger input. The coincidence of two subsequent scintillation logic pulses delayed by a maximum of  $7\ \mu\text{s}$  forms the Michel electron trigger.

## 3.5 Control Systems

LArIAT is a complex ensemble of systems which needed to be monitored at once during data taking. We performed the monitoring of the systems operations with a slow control system, a DAQ monitoring system and a low level data quality monitoring described in the following sections.

### Slow Control

We used the Synoptic Java Web Start framework as a real-time display of subsystem conditions. Its simple Graphical User Interface allowed us to change the operating parameters and to graph the trends of several variables of interest for all the tertiary

beam detectors. Among the most important quantities monitored by Synoptic there are the level of argon in both the inner vessel and the external dewar, the operating voltages of cathode and wire planes, of the PMTs and SiPMs, and of the four wire chambers, as well as the magnets temperature. Figure 3.13 shows an example of the monitoring system. LArIAT uses the Accelerator Control NETwork system (ACNET) to monitor the beam conditions of the MCenter beamline. For example, the horizontal and vertical position of the beam at the first two wire chambers (WC1 and WC2) are shown in 3.14 as seen by the shifter during data taking.

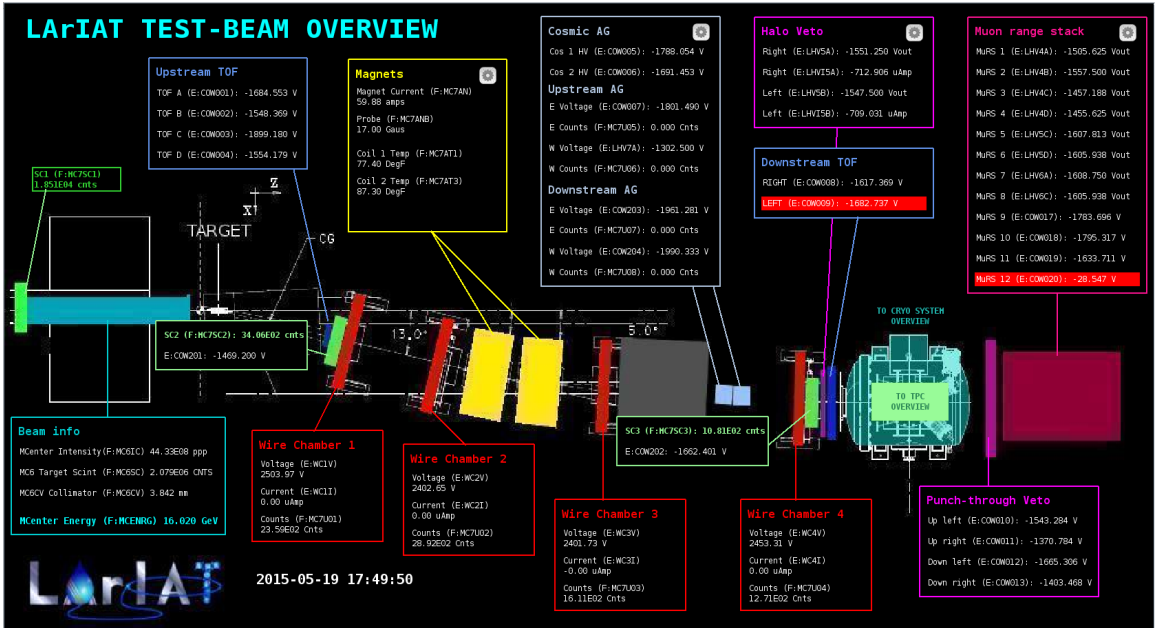


Figure 3.13: Interface of the Synoptic slow control system

## DAQ Monitoring

We monitor the data taking and the run time evolution with the Run Status Webpage (<http://lariat-wbm.fnal.gov/lariat/run.html>), a webpage updated in real-time. The page displays, among other information, the total number of triggers in the event, the total number of detectors triggered during a beam spill, the trigger patterns, the number of times a particular trigger pattern was satisfied during a beam spill, and

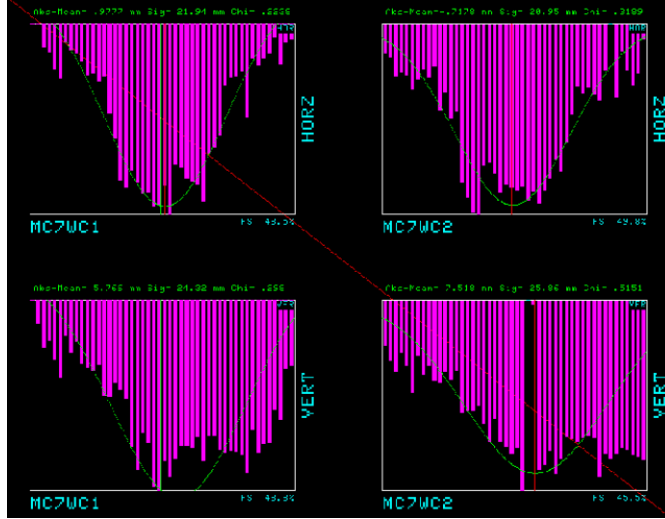


Figure 3.14: Beam position at the upstream wire chambers monitored with ACNET.

the current time relative to the Fermilab accelerator complex supercycle. A screen shot of the page is show in figure 3.15.

## Data Quality Monitoring

We employ two systems to ensure the quality of our data during data taking: the Near-Real-Time Data Quality Monitoring and the Event Viewer.

The Near-Real-Time Data Quality Monitoring (DQM) is a webpage which receives updates from all the VME boards in the trigger system and displays the results of a quick analysis of the DAQ stream of raw data on a spill-by-spill basis. The DQM allows the shifter to monitor almost in real time (typically with a 2-minute delay) a series of low level-quantities and compare them to past collections of beam spills. Some of the variables monitored in the DQM are the pedestal mean and RMS on CAEN digitizer boards of the TPC wires and PMTs of the beamline detectors, the hit occupancy and timing plots on the wire chambers, and number of data fragments recorded that are used to build a TPC event. Abnormal values for low-level quantity in the data activate a series of alarms in the DQM; this quick feedback on the DAQ and beam conditions is fundamental to assure a fast debugging of the detector and a

very efficient data taking during beam uptime.

The online Event Viewer displays a two dimensional representation of LArIAT TPC events on both the Induction and the Collection planes in near real time. The raw pulses collected by the DAQ on each wire are plotted as a function of drift time, resulting in an image of the TPC event easily readable by the shifter. This tool guarantees a particularly good check of the TPC operation which activate an immediate feedback for troubleshooting a number of issues. For example, it is easy for the shifter to spot high occupancy events and request a reduction of the primary beam intensity, or to spot a decrease of the argon purity which requires the regeneration of filters, or to catch the presence of electronic noise and reboot the ASICs. An example of high occupancy event is shown in 3.16.

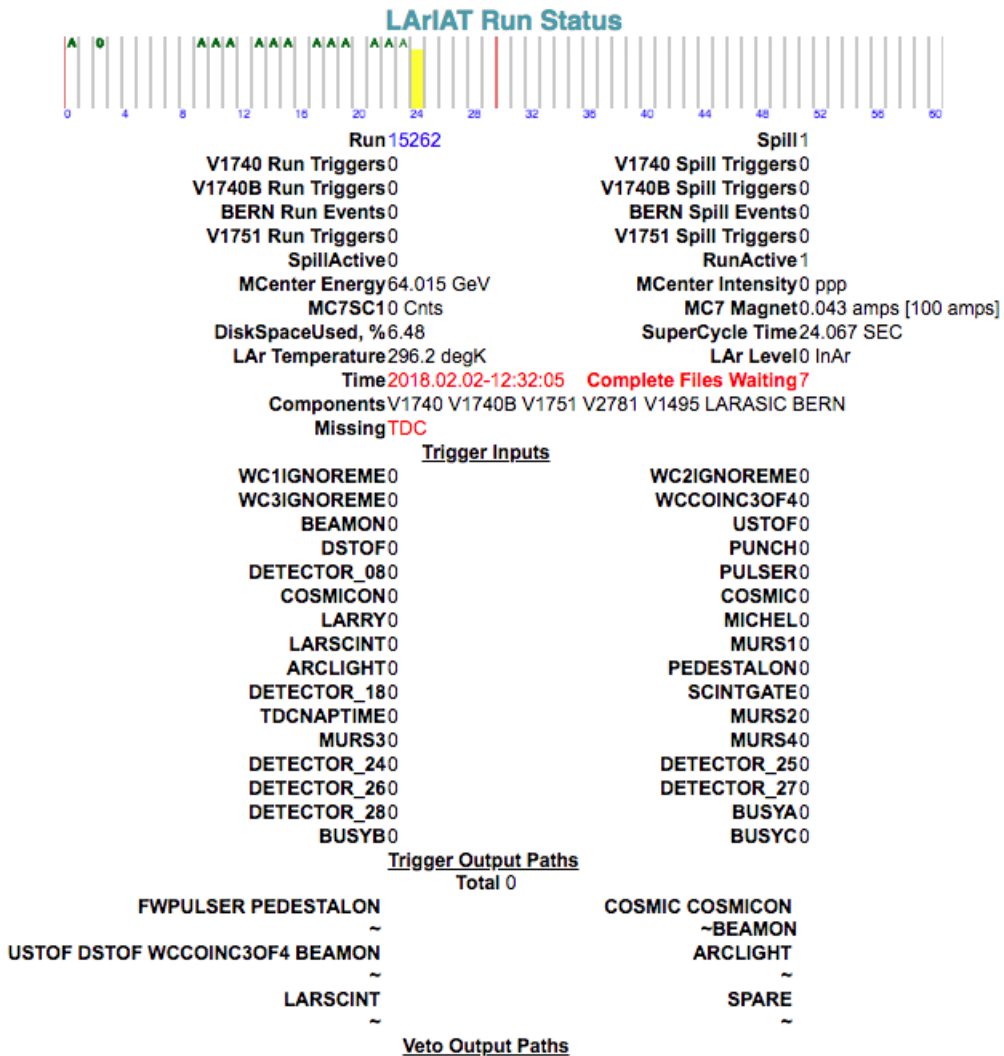


Figure 3.15: Run Status page at LArIAT downtime. At the top the yellow bar displays the current position in the Fermilab supercycle. Interesting information to be monitored by the shifter were the run number and number of spills, time elapsed from data taking (here in red), the energy of the secondary beam and the trigger paths.

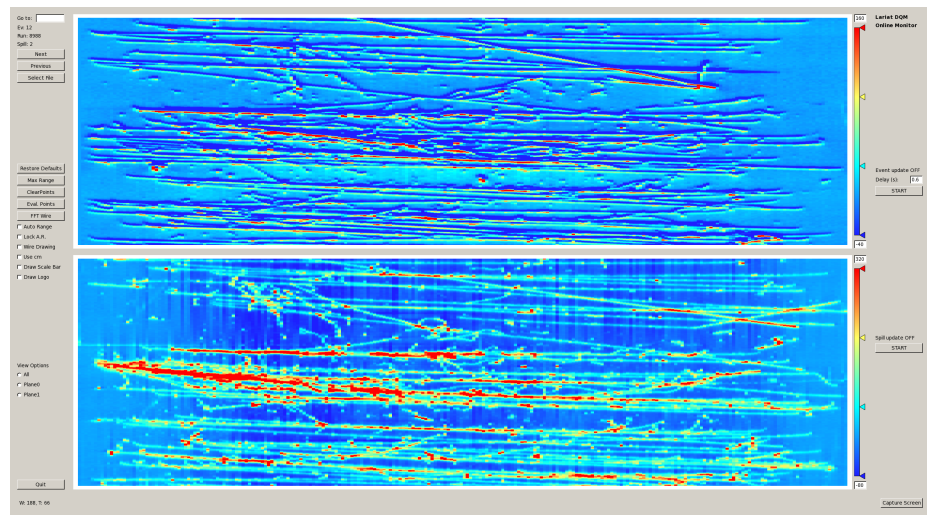


Figure 3.16: High occupancy event display: induction plane (top) and collection plane (bottom).

# Chapter 4

## Hadron Interactions in Argon: Cross Section

### 4.1 How to Measure a Hadron Cross Section in LArIAT

We use both the LArIAT beamline detectors and the LArTPC information to measure hadronic cross sections in argon. Albeit with small differences, both the  $\pi^-$  - Ar and  $K^+$  - Ar total hadronic cross section measurements rely on the same procedure described in details in the following paragraphs: we select the particle of interest using a combination of beamline detectors and TPC information (paragraph 4.1.1), we perform a handshake between the beamline information and the TPC tracking to assure we are selecting the right TPC track (paragraph 4.1.2), and we apply the “thin slice” method to get to the final result (paragraph 4.1.3). We show a cross check of this method in paragraph 4.1.4.

### 4.1.1 Event Selection

#### Beamline events

As will be clear in paragraph 4.1.3, beamline particle identification and momentum measurement before entering the TPC are fundamental information for the hadronic cross sections measurements in LArIAT. Thus, we scan the LArIAT data to keep only events whose wire chamber and time of flight information is registered. Additionally, we perform a check of the plausibility of the trajectory inside the beamline detectors: given the position of the hits in the four wire chambers, we make sure the particle trajectory does not cross any impenetrable material such as the collimator and the magnets steel.

#### Particle Identification in the beamline

In data, the main tool to establish the identity of the hadron of interest is the LArIAT tertiary beamline, in its function of mass spectrometer. We combine the measurement of the time of flight,  $TOF$ , and the beamline momentum,  $p_{Beam}$ , to reconstruct the invariant mass of the particles in the beamline,  $m_{Beam}$ , as follows

$$m_{Beam} = \frac{p_{Beam}}{c} \sqrt{\left(\frac{TOF * c}{l}\right)^2 - 1}, \quad (4.1)$$

where  $c$  is the speed of light and  $l$  is the length of the particle trajectory between the time of flight paddles.

Figure 4.1 shows the mass distribution for the Run II negative polarity runs on the left and positive polarity runs on the right. We perform the classification of events into the different samples as follows:

- $\pi, \mu, e$ :  $0 \text{ MeV} < \text{mass} < 350 \text{ MeV}$
- kaon:  $350 \text{ MeV} < \text{mass} < 650 \text{ MeV}$

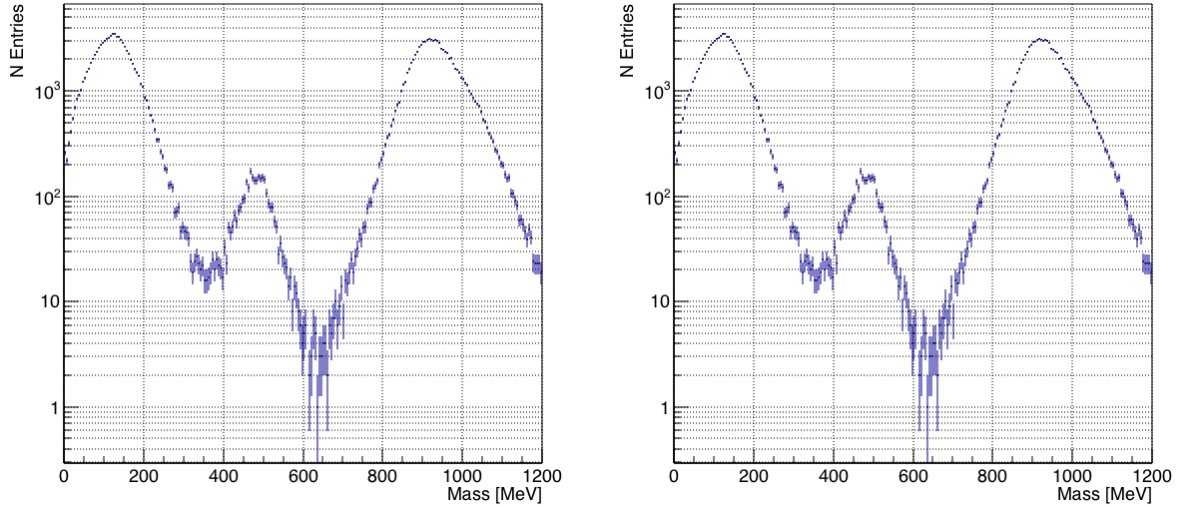


Figure 4.1: The mass plotted for a sample of Run-II events reconstructed in the beamline, negative polarity runs on the left and positive polarity runs on the right. The classification of the events into  $\pi$ ,  $\mu$ ,  $e$ , kaon, or proton is based on this distribution.  
**CHANGE PLOTS**

- proton:  $650 \text{ MeV} < \text{mass} < 3000 \text{ MeV}$ .

### Additional Particle Identification technique

In the case of the  $\pi^-$ -Ar cross section, the resolution of beamline mass spectrometer is not sufficient to select a beam of pure pions. In fact, muons and electrons survive the selection on the beamline mass value. It is important to notice that the composition of the negative polarity beam is mostly pions, as discussed in ???. Anyhow, we devise a selection on the TPC information to mitigate the presence of electrons in the sample used for the pion cross section. The selection relies on the different topologies of a pion and an electron event in the argon: while the former will trace a track inside the TPC active volume, the latter will tend to “shower”, i.e. interact with the medium, produce bremsstrahlung photons which pair convert into several short tracks. We provide details of this selection in section ??.

## Pile up mitigation

The secondary beam impinging on LArIAT secondary target produces a plethora of particles. The presence of upstream and downstream collimators greatly abates the number of particles tracing down the LArIAT beamline. However, more than one beamline particles, or particles produced from the beam interaction with the beamline detectors, may sneak into the LArTPC during its readout time. The TPC readout is triggered by the actual particle firing the beamline detectors; we call “pile up” the additional traces in the TPC. We adjusted the primary beam intensity between LArIAT Run I and Run II to minimize the presence of events with high pile up particles in the data sample. For the cross section analyses, we remove events with more than 4 tracks in the first 14 cm upstream portion of the TPC from the sample.

probably need to do a better job explaining pile up

### 4.1.2 Wire Chamber to TPC Match

For each event passing the selection on its beamline information we need to identify the track inside the TPC corresponding to the particle which triggered the beamline detectors, a procedure we refer to as “WC to TPC match” (WC2TPC for short). In general, the TPC tracking algorithm will reconstruct more than one track in the event, partially due to the fact that hadrons interact in the chamber, as shown in figure ??, and partially because of pile up particles during the triggered TPC drift time, as shown in figure ??.

ADD EVENT DISPLAYS

We attempt to uniquely match one wire chamber track to one and only one reconstructed TPC track. In data, this match leverages on a geometrical selection exploiting both the position of the wire chamber and TPC tracks, and the angle between them. We consider only TPC tracks whose first point is in the first 2 cm upstream portion of the TPC for the match. We project the wire chamber track to the TPC front face where we define the  $x_{FF}$  and  $y_{FF}$  coordinates used for evaluating the

match. We define  $\Delta X$  as the difference between the  $x$  position of the most upstream point of the TPC track and  $x_{FF}$ .  $\Delta Y$  is defined analogously. We define the radius difference,  $\Delta R$ , as  $\Delta R = \sqrt{\Delta X^2 + \Delta Y^2}$ . The angle between the incident WC track and the TPC track in the plane that contains them defines  $\alpha$ . If  $\Delta R < 4$  cm,  $\alpha < 8^\circ$ , a match between WC-track and TPC reconstructed track is found. We describe how we determinate the best value for the radius and angular selection in sec 5.4.1. In MC, we mimic the matching between the WC and the TPC track by constructing a fake WC track using truth information at wire chamber four. We then apply the same WC to TPC matching algorithm as in data. We discard events with multiple WC2TPC matches. We use only TPC track matched to WC tracks in the cross section calculation.

#### 4.1.3 The Thin Slice Method

##### Cross Sections on Thin Target

Cross section measurements on a thin target have been the bread and butter of nuclear and particle experimentalists since the Rutherford experiments NEED CITATION. At their core, this type of experiments consists in shooting a beam of particles with a known flux on a thin target and recording the outgoing flux.

In general, the target is not a single particle, but rather a slab of material containing many diffusion centers. The so-called “thin target” approximation assumes that the target centers are uniformly distributed in the material and that the target is thin compared to the interaction length so that no center of interaction sits in front of another. In this approximation, the ratio between the number of particles interacting in the target  $N_{Interacting}$  and number of incident particles  $N_{Incident}$  determines the interaction probability  $P_{Interacting}$ , which is the complementary to one of the survival

probability  $P_{Survival}$ . Equation 4.2

$$P_{Survival} = 1 - P_{Interacting} = 1 - \frac{N_{Interacting}}{N_{Incident}} = e^{-\sigma_{TOT} n \delta X} \quad (4.2)$$

describes the probability for a particle to survive the thin target. This formula relates the total cross section  $\sigma_{TOT}$ , the density of the target centers  $n$  and the thickness of the target along the incident hadron direction  $\delta X$ , to the interaction probability<sup>1</sup>. If the target is thin compared to the interaction length of the process considered, we can Taylor expand the exponential function in equation 4.2 and find a simple proportionality relationship between the number of incident and interacting particles, and the cross section, as shown in equation 4.3:

$$1 - \frac{N_{Interacting}}{N_{Incident}} = 1 - \sigma_{TOT} n \delta X + O(\delta X^2). \quad (4.3)$$

Solving for the cross section, we find:

$$\sigma_{TOT} = \frac{1}{n \delta X} \frac{N_{Interacting}}{N_{Incident}}. \quad (4.4)$$

### Not-so-Thin Target: Slicing the Argon

The LArIAT TPC, with its 90 cm of length, is not a thin target. Find expected interaction length for hadrons and kaons. However, the fine-grained tracking of the LArIAT LArTPC allows us to treat the argon volume as a sequence of many adjacent thin targets.

As described in section 3, LArIAT wire planes count 240 wires each. The wires are oriented at +/- 60° from the vertical direction at 4 mm spacing, while the beam direction is oriented 3 degrees off the  $z$  axis in the  $XZ$  plane. review this math The

---

<sup>1</sup>. The scattering center density in the target,  $n$ , relates to the argon density  $\rho$ , the Avogadro number  $N_A$  and the argon molar mass  $m_A$  as  $n = \frac{\rho N_A}{m_A}$ .

wires collect signals proportional to the energy loss of the hadron along its path in a  $\delta X = 4 \text{ mm}/\sin(60^\circ) \approx 4.7 \text{ mm}$  slab of liquid argon. Thus, one can think to slice the TPC into many thin targets of  $\delta X = 4.7 \text{ mm}$  thickness along the direction of the incident particle.

Considering each slice  $j$  a “thin target”, we can apply the cross section calculation from Eq. 4.4 iteratively, evaluating the kinetic energy of the hadron as it enters each slice,  $E_j^{kin}$ . For each WC-to-TPC matched particle, the energy of the hadron entering the TPC is known thanks to the momentum and mass determination by the tertiary beamline,

$$E_{FrontFace}^{kin} = \sqrt{p_{Beam}^2 - m_{Beam}^2} - m_{Beam} - E_{loss}, \quad (4.5)$$

where  $E_{loss}$  is a correction for the energy loss in the dead material between the beamline and the TPC front face (more on ??). The energy of the hadron at the each slab is determined by subtracting the energy released by the particle in the previous slabs. For example, at the  $j^{th}$  point of a track, the kinetic energy will be

$$E_j^{kin} = E_{FrontFace}^{kin} - \sum_{i < j} \Delta E_i, \quad (4.6)$$

where  $\Delta E_i$  is the energy deposited at each argon slice before the  $j^{th}$  point as measured by the calorimetry associated with the tracking.

If the particle enters a slice, it contributes to  $N_{Incident}(E^{kin})$  in the energy bin corresponding to its kinetic energy in that slice. If it interacts in the slice, it then also contributes to  $N_{Interacting}(E^{kin})$  in the appropriate energy bin. The cross section as a function of kinetic energy,  $\sigma_{TOT}(E^{kin})$  will then be proportional to the ratio  $\frac{N_{Interacting}(E^{kin})}{N_{Incident}(E^{kin})}$ .

The statistical uncertainty for each energy bin is calculated by error propagation from the statistical uncertainty on  $N_{Incident}$  and  $N_{Interacting}$ . Since the number of

incident hadrons in each energy bin is given by a simple counting, we assume that  $N_{Incident}$  is distributed as a poissonian with mean and  $\sigma^2$  equal to  $N_{Incident}$  in each bin. On the other hand,  $N_{Interacting}$  follows a binomial distribution: a particle in a given energy bin might or might not interact. The square of the variance for the binomial is given by

$$\sigma^2 = \mathcal{N}P_{Interacting}(1 - P_{Interacting}); \quad (4.7)$$

since the interaction probability  $P_{Interacting}$  is  $\frac{N_{Interacting}}{N_{Incident}}$  and the number of tries  $\mathcal{N}$  is  $N_{Incident}$ , equation 4.7 translates into

$$\sigma^2 = N_{Incident} \frac{N_{Interacting}}{N_{Incident}} \left(1 - \frac{N_{Interacting}}{N_{Incident}}\right) = N_{Interacting} \left(1 - \frac{N_{Interacting}}{N_{Incident}}\right). \quad (4.8)$$

$N_{Incident}$  and  $N_{Interacting}$  are not independent. The uncertainty on the cross section is thus calculated as

$$\delta\sigma_{tot}(E) = \sigma_{tot}(E) \left( \frac{\delta N_{Interacting}}{N_{Interacting}} + \frac{\delta N_{Incident}}{N_{Incident}} \right) \quad (4.9)$$

where:

$$\delta N_{Incident} = \sqrt{N_{Incident}} \quad (4.10)$$

$$\delta N_{Interacting} = \sqrt{N_{Interacting} \left(1 - \frac{N_{Interacting}}{N_{Incident}}\right)}. \quad (4.11)$$

#### 4.1.4 Procedure testing with truth quantities

The  $\pi^-$ -Ar and  $K^+$ -Ar total hadronic cross section implemented in Geant4 can be used as a tool to validate the measurement methodology. We describe here a closure test done on Monte Carlo to prove that the methodology of slicing the TPC retrieves the underlying cross section distribution implemented in Geant4 within the statistical error.

For pions in the considered energy range, the Geant4 inelastic model adopted to is “BertiniCascade”, while the elastic model “hElasticLHEP”. For kaons, the Geant4 inelastic model adopted to is “BertiniCascade”, while the elastic model “hElasticLHEP”.

For the validation test, we fire about 390000 pions and 140000 kaons inside the LArIAT TPC active volume using the DDMC (see sec ??). We apply the thin-sliced method on using true quantities to calculate the hadron kinetic energy at each slab in order to decouple reconstruction effects to eventual issues with the methodology. For each slab of 4.7 mm length on the path of the hadron, we integrate the true energy deposition as given by the Geant4 transportation model. Then, we recursively subtracted it from the hadron kinetic energy at the TPC front face to evaluate the kinetic energy at each slab until the true interaction point is reached. Doing so, we obtain the true interacting and incident distributions for the considered hadron and we obtain the true MC cross section as a function of the hadron true kinetic energy.

Figure ?? shows the total hadronic cross section for argon implemented in Geant4 10.01.p3 (solid lines) overlaid with the true MC cross section as obtained with the sliced TPC method (markers) for pions on the left and kaons on the right; the total cross section is shown in green, the elastic cross section in blue and the inelastic cross section in red. The nice agreement with the Geant4 distribution and the cross section obtained with the sliced TPC method gives us confidence in the validity of the methodology.

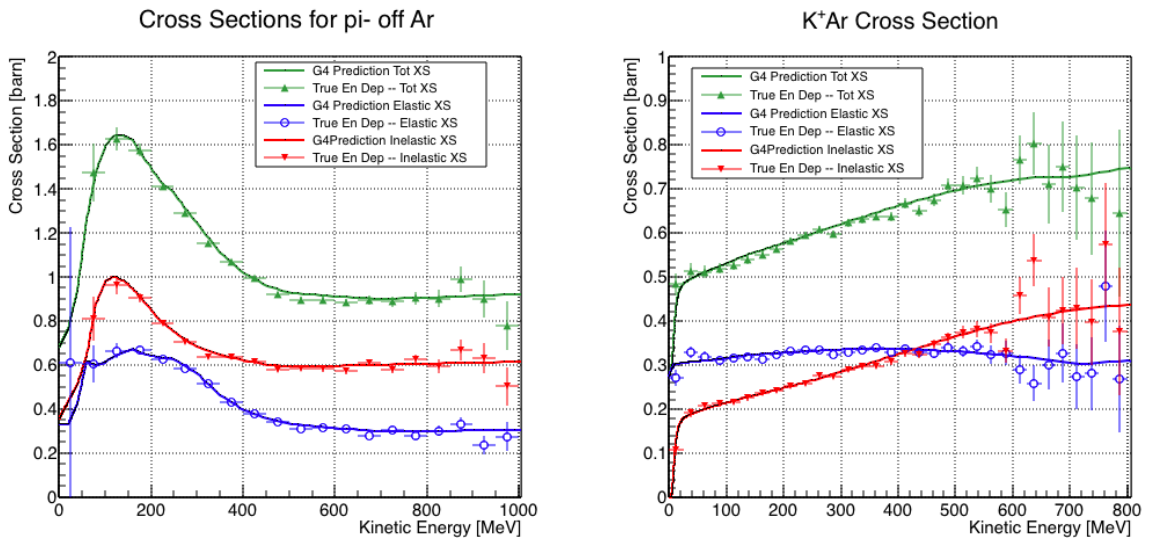


Figure 4.2: Hadronic cross sections for  $\pi^-$ -Ar (left) and  $K^+$ -Ar (right) implemented in Geant4 10.01.p3 (solid lines) overlaid the true MC cross section as obtained with the sliced TPC method (markers). The total cross section is shown in green, the elastic cross section in blue and the inelastic cross section in red.

# **Chapter 5**

## **Samples Preparation**

This chapter describes the data and Monte Carlo samples used for the cross section analyses,

### **5.1 LArIAT Data**

### **5.2 LArIAT Monte Carlo**

#### **5.2.1 G4Beamline**

#### **5.2.2 Data Driven MC**

### **5.3 Energy Calibration**

### **5.4 Tracking Studies**

In this section, we describe three studies. The first is a justification of the selection criteria for the beamline handshake with the TPC information. We perform this study to boost the correct identification of the particles in the TPC associated with

the beamline information, while maintaining sufficient statistics for the cross section measurement. The second study is an optimization of the tracking algorithm, with the scope of maximizing the identification of the hadronic interaction point inside the TPC. These two studies are related, since the optimization of the tracking is performed on TPC tracks which have been matched to the wire chamber track; in turn, the tracking algorithm for TPC tracks determine the number of reconstructed tracks in each event used to try the matching with the wire chamber track. Starting with a sensible tracking reconstruction, we perform the WC2TPC matching optimization first, then the tracking optimization. The WC2TPC match purity and efficiency are then calculated again with the optimized tracking.

We perform the following studies on a MC sample of 191000 kaons and 359000 pions produced with the DDMC technique. DDMC particles are shot from the WC4 location into the TPC following the beam profile. We mimic the matching between the WC and the TPC track on Monte Carlo by constructing a fake WC track using truth information at wire chamber four. We then apply the same WC to TPC matching algorithm as in data described in 4.1.2.

#### 5.4.1 Selection Study for the Wire Chamber to TPC Match

Plots I want in this section:

1. WC2TPC MC DeltaX, DeltaY and  $\alpha$

Scope of this study is assessing the goodness of the wire chamber to TPC match on Monte Carlo and decide the selection values we will use on data. A word of caution is necessary here. With this study, we want to minimize pathologies associated with the presence of the primary hadron itself, e.g. the incorrect association between the beamline hadron and its decay products inside the TPC. Assessing the contamination from pile-up<sup>1</sup>, albeit related, is beyond the scope of this study.

---

1. We remind the reader that the DDMC is a single particle Monte Carlo, where the beam pile

In MC, we are able to define a correct WC2TPC match using the Geant4 truth information. We are thus able to count how many times the WC tracks is associated with the wrong TPC reconstructed track.

We define a correct match if the all following conditions are met:

- the length of the true primary Geant4 track in the TPC is greater than 2 cm,
- the length of the reconstructed track length is greater than 2 cm,
- the Z position of the first reconstructed point is within 2 cm from the TPC front face
- the distance between the reconstructed track and the true entering point is the minimum compared with all the other reconstructed tracks.

In order to count the wrong matches, we consider all the reconstructed tracks whose Z position of the first reconstructed point lies within 2 cm from the TPC front face. Events with true length in TPC  $< 2$  cm are included. Since hadrons are shot 100 cm upstream from the TPC front face, the following two scenarios are possible from a truth standpoint:

[*Ta*] the primary hadron decays or interact strongly before getting to the TPC,

[*Tb*] the primary hadron enters the TPC.

Once we choose the selection cuts to determine a reconstructed wire chamber-to-TPC match  $r_T$  and  $\alpha_T$ , the following five scenarios are possible in the truth to reconstruction interplay :

- 1) only the correct track is matched
- 2) only one wrong track is matched

---

up is not simulated.

- 3) the correct track and one (or more) wrong tracks are matched
- 4) multiple wrong tracks matched.
- 5) no reconstructed tracks are matched

Since we keep only events with one and only one match, we discard cases 3), 4) and 5) from the events used in the cross section measurement. For each set of  $r_T$  and  $\alpha_T$  selection value, we define purity and efficiency of the selection as follows:

$$\text{Efficiency} = \frac{\text{Number of events correctly matched}}{\text{Number of events with primary in TPC}} \quad (5.1)$$

$$\text{Purity} = \frac{\text{Number of events correctly matched}}{\text{Total number of matched events}}. \quad (5.2)$$

Figure 5.1 shows the efficiency (left) and purity (right) for wire chamber-to-TPC match as a function of the radius,  $r_T$ , and angle,  $\alpha_T$ , selection value. It is apparent how both efficiency and purity are fairly flat as a function of the radius selection value at a given angle. This is not surprising. Since we are studying a single particle gun Monte Carlo sample, the wrong matches can occur only for mis-tracking of the primary or for association with decay products; decay products will tend to be produced at large angles compared to the primary, but could be fairly close to the in  $x$  and  $y$  projection of the primary. The radius cut would play a key role in removing pile up events.

For LArIAT cross section measurements, we generally prefer purity over efficiency, since a sample of particles of a pure species will lead to a better measurement. Obviously, purity should be balanced with a sensible efficiency to avoid rejecting the whole sample.

We choose  $(\alpha_T, r_T) = (8 \text{ deg}, 4 \text{ cm})$  and get a MC 85% efficiency and 98% purity for the kaon sample and a MC BOH% efficiency and 98% purity for the BOH sample.

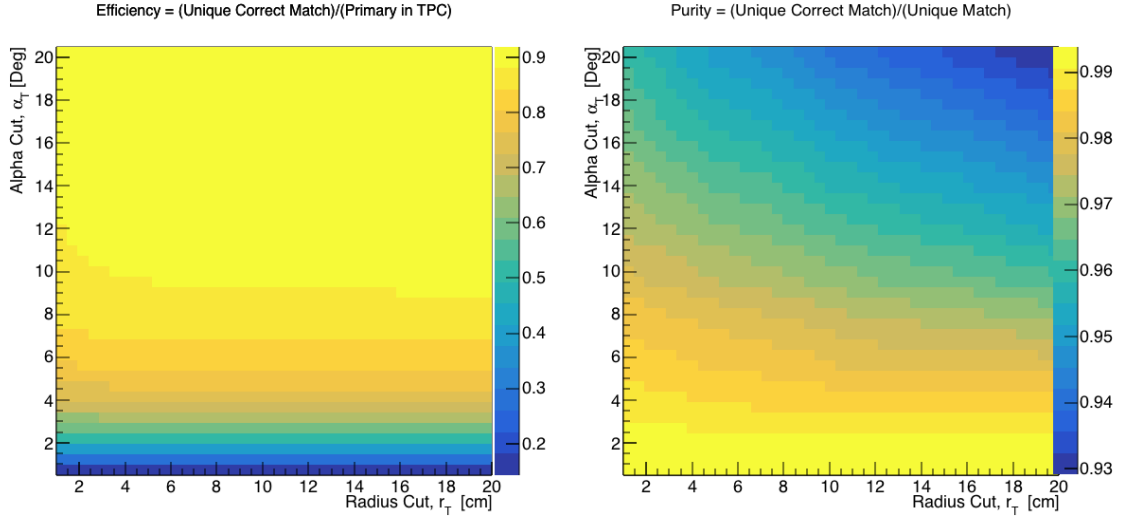


Figure 5.1: Efficiency (left) and purity (right) for wire chamber-to-TPC match as a function of the radius and angle selections.

### 5.4.2 Interaction Point Optimization

Scheme of this subsection

**Brief Explanation of the reconstruction chain**

**Explanation of clustering parameters**

**Figure of merit and spanning of cluster**

**Important numbers out of this optimization**

Plots I want in this section:

1. Delta L, reco - true
2. Delta L, reco - true Elastic, Delta L, reco - true Inelastic, other
3. Length Quality cut
4. Efficiency as a function of true KE and Angle

### 5.4.3 Tracking spatial and angular resolution

Scope of this study is understanding and comparing the tracking spatial and angular resolution on data and MC. We start by selecting all the WC2TPC matched tracks. We fit a line on all the space points of the track and calculate the  $\chi^2$ . The  $\chi^2$  distribution for data and MC is shown in Figure ??.

For the spatial and angular resolution study, we reject tracks with less than 14 space points. For each track, we order the space points according to their Z position and we split them in two sets: the first set counts all the points belonging to the first half of the track and the second set counts all the points belonging to the second half of the track. We remove the last 5 points in the first set and the first 5 points in the second set, so to have a gap in the middle of the original track. We fit the first and the second set of points with a line separately. We reject the event entirely if the  $\chi^2$  for the fit of either of the halves is greater than four. We define a track middle plane as the plane perpendicular to the original track fit, positioned in the middle of its length. We project the tracks on the middle plane and calculate the impact parameter,  $d$ , i.e. the distance between the projected points. We also calculate the angle between the original track direction and the fit of the first and second half, called  $\alpha_1$  and  $\alpha_2$  respectively. The spatial resolution of the track will be  $\sigma_S = \frac{d}{\sqrt{2}}$  while the angular resolution of the tracks will be  $\sigma_\alpha = \alpha_1 - \alpha_2$ . The distributions for data and MC for  $\sigma_\alpha$  and  $\sigma_S$  are given in ??.

# Chapter 6

## Background subtraction

### 6.1 Assessing Beamline Contamination

What is the beamline contamination? We define beamline contamination every TPC track matched to the WC track which is not a primary pion. There are 4 different types of beamline contaminations:

- 1) electrons,
- 2) muons,
- 3) secondaries from pion events,
- 4) matched pile up events.

So, how do we handle this contamination? The first step is to estimate what percentage of events used in the cross section calculation is not a primary pion.

#### 6.1.1 Electron and Muon contamination

We estimate the percentage of electrons and muons in the beam via the beamline MC. Since the beamline composition is a function of the magnet settings, we simulate separately events for magnet current of -60A and -100A.

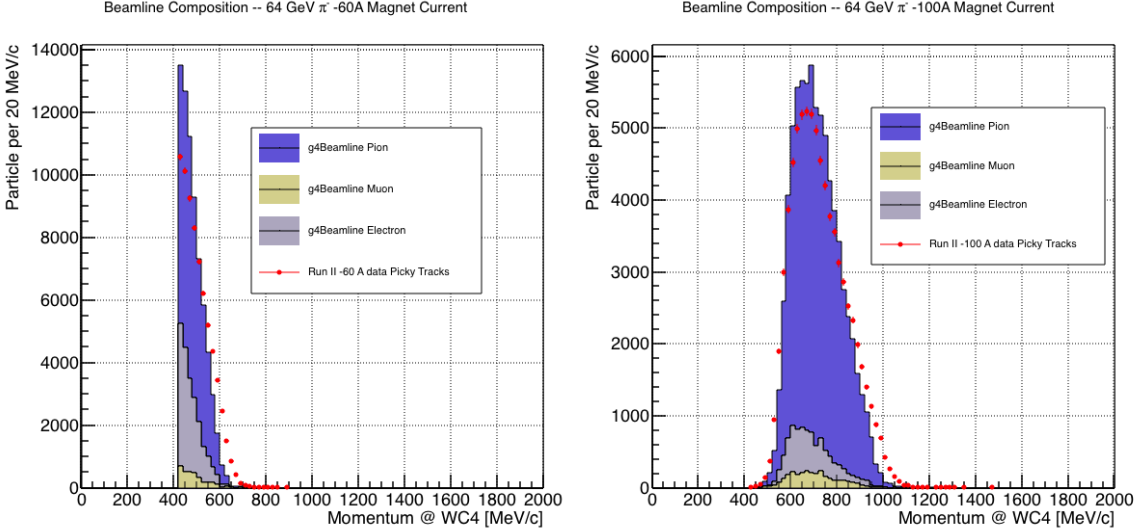


Figure 6.1: Beam composition for the -60A runs (left) and -100A runs (right). The solid blue plot represents the pion content, the yellow plot represents the muon content and the grey plot represents the electron content. The plots are area normalized to the number of data events, shown in red.

	I = -60 A	I = -100 A
G4Pions	68.8 %	87.4 %
G4Muons	4.6 %	3.7 %
G4Electrons	26.6 %	8.9 %

Table 6.1: Beamline composition per magnet settings

Table ?? shows the beam composition per magnet setting after the mass selection according to the G4simulation,

We calculate the electron to pion and muon to pion ratio on the whole sample as the weighted sum of the corresponding ratio in the two current settings,

$$\frac{N_e}{N_{\pi \text{ Data}}} = w_{60A} \frac{N_e}{N_{\pi 60A}} + w_{100A} \frac{N_e}{N_{\pi 100A}}, \quad (6.1)$$

$$\frac{N_\mu}{N_{\pi \text{ Data}}} = w_{60A} \frac{N_\mu}{N_{\pi 60A}} + w_{100A} \frac{N_\mu}{N_{\pi 100A}}, \quad (6.2)$$

where the weights  $w_{60A}$  and  $w_{100A}$  are the percentage of events in the corresponding magnet configuration passing the mass selection in data, as shown in ??.

	I = -60 A	I = -100 A	Total	w <sub>60A</sub>	w <sub>100A</sub>
Data events after Mass Cut	70192	76056	146248	0.48	0.52
Data events for Cross Section					
Estimated e number	18671.1	6769.0			
Estimated $\mu$ number	3228.8	2814.1			
Estimated $\pi$ number	48292.1	66472.9			

Table 6.2: Data events per magnet settings

Once the beam composition is known, we simulate the electrons, muons and pions with the DDMC and we subject the three samples to the same selection chain (WC2TPC match, shower filter, pile up filter, etc...). The percentage of electrons and muons surviving the selection chain is the electron and muon contamination in the pion cross section sample.

### 6.1.2 Contamination from secondaries

The percentage of secondaries is given in the MC by the number of matched WC2TPC tracks which are not flagged as primary by Geant4. We estimate the last type of contamination, the “matched pile up” events, to be a negligible fraction, because of the definition of the WC2TPC match: we deem the probability of a single match with a halo particle in the absence of a beamline particle<sup>1</sup> extremely small.

## 6.2 Subtraction

Once we estimate the contaminants to primary pion ratio, the next step is subtracting their contribution from data for each type of contaminant independently. The contaminant samples are reconstructed and the corresponding interacting and incident histograms are produced. We then perform a bin by bin subtraction in the data interacting and incident histograms separately. A graphical rendering of this

---

1. Events with multiple WC2TPC matches are always rejected.

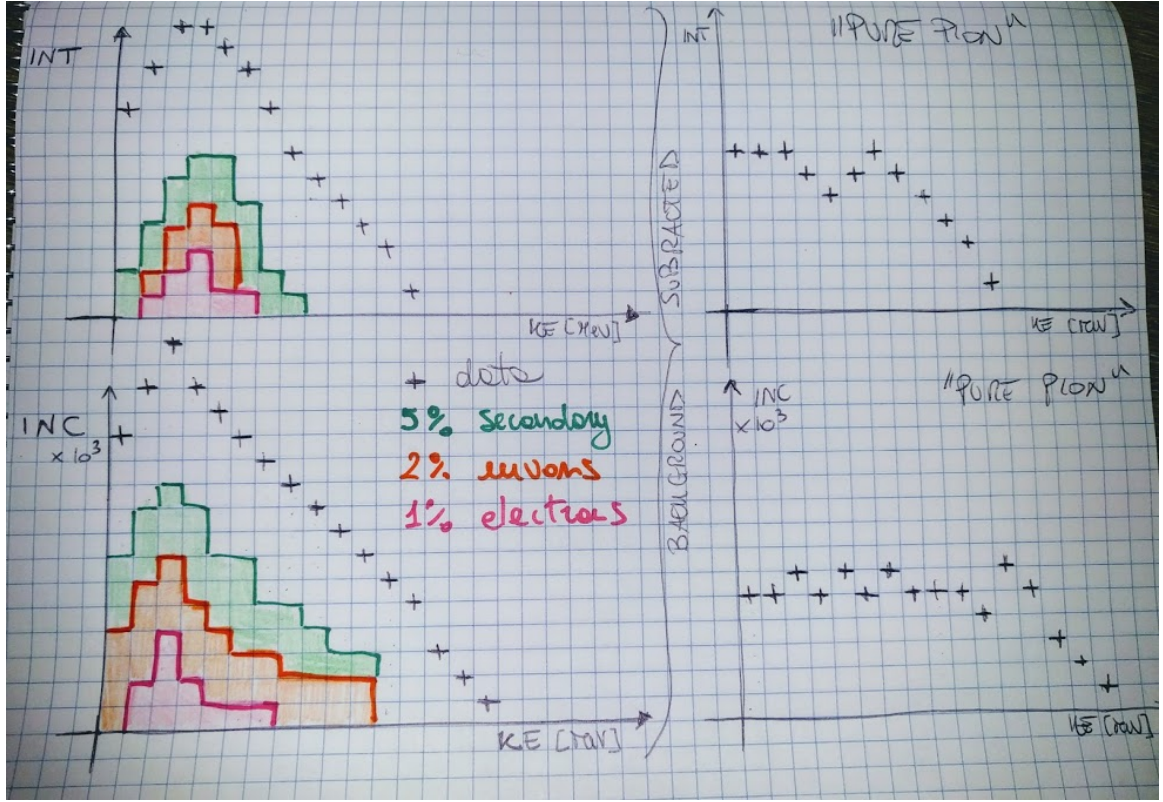


Figure 6.2: A graphical rendering of the beamline contamination background subtraction. The contribution of the contaminants is shown in green for the secondaries, in orange for the muons and in pink for electrons. The colored plots are coming from the MC and are staggered. The percentages shown in the legend are the percentages of contaminants over the total number of events passing the selection chain. We actually expect way less contamination.

procedure is shown in Fig ?? Once the data is background subtracted, we apply the correction laid out in the previous section. [How do we account for the error in the contamination subtraction?](#) We change the electron/pion and muon/pion ratio and we see how much difference we get?

### 6.3 Capture and decay

Our goal is to measure the total hadronic cross section for negative pions in argon. Since pion capture can be classified as an electromagnetic process and pion decay is a

weak process, capture and decay represent unwanted interactions. We present here a study of capture and decay in Monte Carlo and the solution we adopted to mitigate their presence in the data sample.

For this MC study, we use a sample of 359000 MC pions generated according to the beam profile with the DDMC described in 5.2.2. It is important to notice that capture occurs predominantly at rest, while decay may occur both in flight and at rest. Thus, we can highly mitigate capture and decay at rest by removing pions which would release all their energy in the TPC and stop. This translates into a momentum selection, where we keep only events whose WC momentum is above a certain threshold. Figure 6.3 shows the true momentum distribution for the primary<sup>2</sup> pions that arrive to the TPC (pink), that capture (green) or decay (blue) inside the TPC, on a linear and log scale vertical axis.

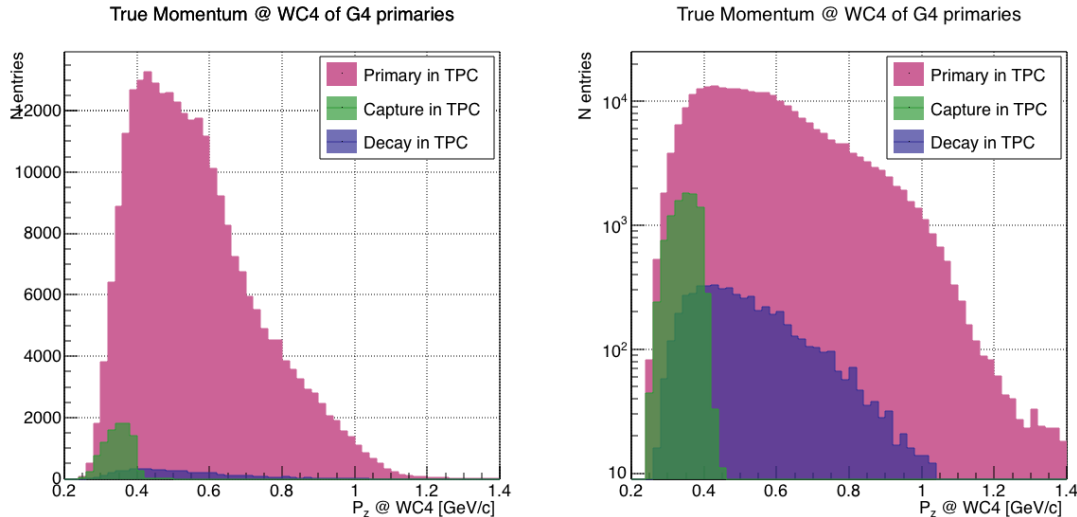


Figure 6.3: True momentum distribution at wire chamber 4 for every simulated pion arriving in the TPC (pink), ending its life in capture (green) or in decay (blue) in the TPC, linear vertical axis on the left, logarithmic on the right.

In order to choose the selection value for the wire chamber momentum, it is

---

2. We use here the Geant4 denomination “primary” to indicate that the pion considered does not undergo interactions modifying its energy before getting to the TPC. In fact, not every pion shot from wire chamber four will arrive to the TPC as primary, some will decay or interact before the TPC.

beneficial to estimate the ratio of events which capture or decay that survive the selection in MC as a function of the momentum threshold, and compare it with the survival ratio for all events. This is done in figure 6.4. We define the survival ratio simply as the number of events surviving the true momentum selection divided by the number of events of that category. We calculate the survival ratio separately for the three event categories explained above: total (pink), capture (green) and decay (blue). Selecting pions with momentum greater than 420 MeV/c reduces the capture events by 99% while maintaining about 80% of the total data sample. Figure 6.5 shows the ratio of events which end their life in capture (green) or decay (blue) over the total number of events as a function of the true momentum at wire chamber four. This ratio is slightly dependent on the inelastic cross section implemented in Geant4, as we are able to register a pion capture (or decay) only if it did not interact inelastically in the TPC. We choose a momentum threshold of 420 MeV/c because the percentage of capture events drops below 1% and the percentage of decays is never above 2% for momenta greater than 420 MeV/c.

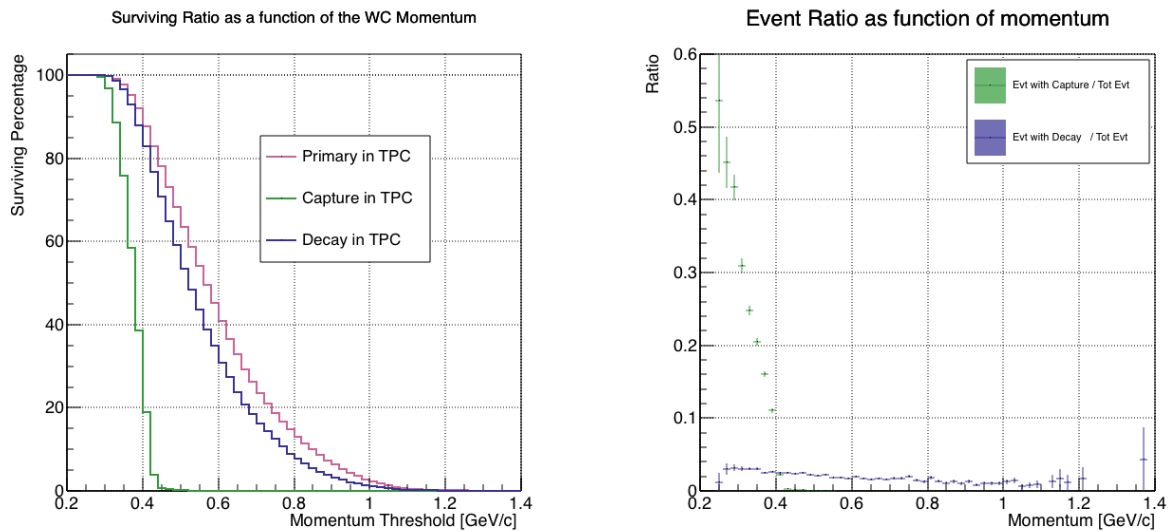


Figure 6.4: Survival ratio as a function of selection threshold on true momentum at wire chamber four for every simulated pion arriving in the TPC (pink), capture (green) or in decay (blue).

Figure 6.5: Ratio between the capture (green) and decay (blue) events over the total number of events as a function of the true momentum at wire chamber four.

# **Chapter 7**

## **Negative Pion Cross Section Measurement**

Your first chapter is probably an introduction. But who knows.

# Chapter 8

## Uncertainty budget

Measuring an hadronic cross section in LArIAT translates into counting how many hadrons impinged on a slab of argon at a given energy and how many of those hadrons interacted at said energy. So, the key questions here are:

- a) how well do we know the kinetic energy at each point of the tracking?
- b) how well do we know when the tracking stops?
- c) are there any systematic shifts?

In order to answer this question, will discuss first a simple scenario were our beam is 100% made of pions which arrive as primaries in the TPC (no decay in the beam and no inelastic interaction before the TPC front face). We will then add a layer of complexity by discussing how we handle beamline contamination.

### 8.1 Pure beam of pions

Assuming a beam of pure pions gets to the TPC, let us explicit some of the variables in the kinetic energy equation 4.6 to point out the important quantities in the uncertainty budget,

$$E_j^{kin} = E_{Beam}^{kin} - E_{loss} - \sum_{i < j} \frac{dE_i}{dx_i} * dx_i \quad (8.1)$$

$$= \sqrt{p_{Beam}^2 - m_{Beam}^2} - m_{Beam} - E_{loss} - \sum_{i < j} \frac{dE_i}{dx_i} * dx_i. \quad (8.2)$$

### 8.1.1 Uncertainty on $E_{Beam}^{kin}$

Let us start by discussing the uncertainty on  $E_{Beam}^{kin}$ . Since we are assuming a beam of pions, the uncertainty on the value of mass of the pion ( $m_{Beam}$ ) as given by the pdg is irrelevant compared to the momentum uncertainties, thus  $\delta E_{Beam}^{kin} = \delta p_{Beam}^{kin}$ . We estimate the momentum uncertainty as follows.

We estimate the uncertainty on a 4-point track. In case of 3-points track, we add an additional 2% coming from Greg's study. Uncertainty on a 4-point track:

- Alignment surveys. 1mm misalignment translates to 3% in overall
- Doug study dp/p = 2% based on field map (docdb 1710)
- Minerva test beam paper

### 8.1.2 Uncertainty on $E_{loss}$

We estimate the uncertainty on the energy loss between the beamline momentum measurement and the TPC,  $E_{loss}$ , using the DDMC pion sample. We shoot pions from WC4 with the same momentum distribution as in the beamline data and plot the true  $E_{loss}$  for that sample. The width of the  $E_{loss}$  distribution is the  $\delta E_{loss}$ .

TO DO HERE: make sure we have the geometry right, cause otherwise this correction is meaningless. With this method, so far we get a mean 40 MeV, but uncertainty 7MeV. The trajectory method does not improve uncertainty, why? It's a mystery I

don't think we should solve before June :). Back of the envelope material budget calculation:

Table 8.1: Back of the envelope calculation

dEdx for MIP, MPV [MeV cm <sup>2</sup> /gr]	density [g/cm <sup>3</sup> ]	width [cm]	E <sub>loss</sub> [MeV]
1.6	1.7 (G10)	1.3	3.5
1.6	1.4 (LAr)	1.77	4.0
1.6	7.7 (S.S.)	0.23	2.8
1.6	4.5 (Ti)	0.04	0.3
1.6	1.03 (Plastic Sci)	1.1	1.8
Total			12.4

Event taking into account a 3 degree bent, we get 12.41 MeV, which is quite far from 40 MeV... something smells here ;)

### 8.1.3 Uncertainty on dE/dx and pitch

We obtain the uncertainty on dE/dx and track pitch by comparing the dE/dx and pitch distributions in data and MC. Currently, MPV MC = 1.70 and MPV DATA = 1.72 MeV/cm ( 3% higher). TO DO HERE: calculate Argon density from mid-RTD temperature. Compare this density with MC Argon density. Density change affects dE/dx (in MeV/cm!). Try changing MC density up to “real one” and see if dEdX agrees between DATA and MC

### 8.1.4 Uncertainty on track end, aka efficiency correction

From the MC, we obtain an efficiency correction on the interacting and incident distributions separately. This is done by comparing the MC reconstructed with the true MC deposition on an event by event basis. This correction is applied bin by bin on the data interacting and incident distributions. The better our tracking, the smaller this efficiency correction will be. So, step number one is improving the tracking. Need to talk to Bruce about this. I don't understand the angle cut that Dave Schmitz and Jon Paley were so vocal about.

Now, the key question remains: does the tracking behave in the same way in data and MC? We can compare some key plots between reconstructed data and MC which gives us confidence this is true: the track pitch, the tracks straightness and the goodness of fit in data and MC. Does such a variable as “goodness of fit” exists in the tracking? We should ask Bruce.

## Appendix A

# Measurement of LArIAT Electric Field

The electric field of a LArTPC in the drift volume is a fundamental quantity for the proper functionality of this technology, as it affects almost every reconstructed quantity such as the position of hits or their collected charge. Given its importance, we calculate the electric field for LArIAT with a single line diagram from our HV circuit and we cross check the obtained value with a measurement relying only on TPC data.

Before getting into the details of the measurement procedures, it is important to explicit the relationship between some quantities in play. The electric field and the drift velocity ( $v_{drift}$ ) are related as follows

$$v_{drift} = \mu(E_{field}, T)E_{field}, \quad (\text{A.1})$$

where  $\mu$  is the electron mobility, which depends on the electric field and on the temperature (T). The empirical formula for this dependency is described in [?] and shown in Figure A.1 for several argon temperatures.

The relationship between the drift time ( $t_{drift}$ ) and the drift velocity is trivially

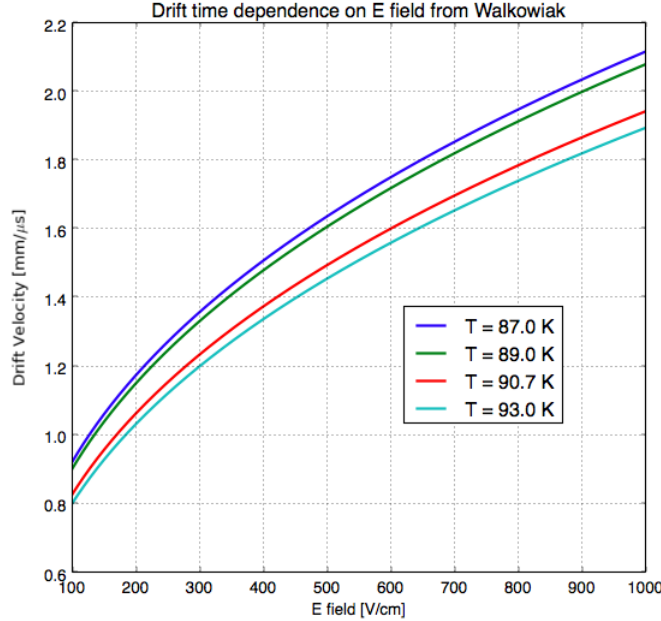


Figure A.1: Drift velocity dependence on electric field for several temperatures. The slope of the line at any one point represents the electron mobility for that given temperature and electric field.

Table A.1: Electric field and drift velocities in LArIAT smaller drift volumes

	Shield-Induction	Induction-Collection
$E_{filed}$	700.625 V/cm	892.5 V/cm
$v_{drift}$	1.73 mm/μs	1.90 mm/μs
$t_{drift}$	2.31 μs	2.11 μs

given by

$$t_{drift} = \Delta x / v_{drift}, \quad (\text{A.2})$$

where  $\Delta x$  is the distance between the edges of the drift region. Table A.1 reports the values of the electric field, drift velocity, and drift times for the smaller drift volumes.

With these basic parameters established, we can now move on to calculating the electric field in the main drift region (between the cathode and the shield plane).

## Single line diagram method

The electric field strength in the LArIAT main drift volume can be determined knowing the voltage applied to the cathode, the voltage applied at the shield plane, and the distance between them. We assume the distance between the cathode and the shield plane to be 470 mm and any length contraction due to the liquid argon is negligibly small ( $\sim 2$  mm).

The voltage applied to the cathode can be calculated using Ohm's law and the single line diagram shown in Figure A.2. A set of two filter pots for emergency power dissipation are positioned between the Glassman power supply and the cathode, one at each end of the feeder cable, each with an internal resistance of  $40 \text{ M}\Omega$ . The output current of the Glassman power supply is then used to determine the electric field strength. Figure A.3 shows an average current of 0.004172 mA from the Glassman power supply.

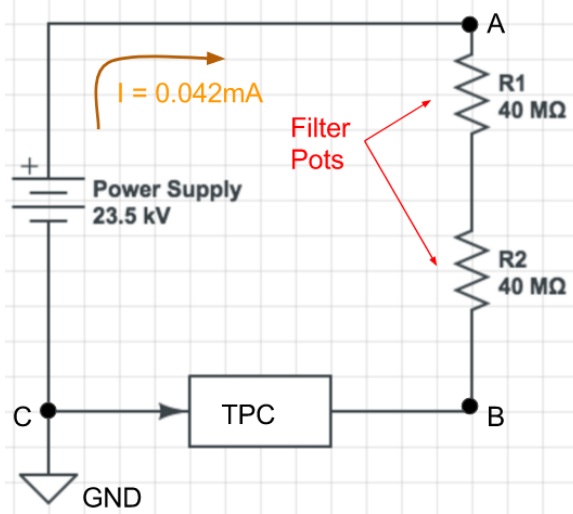


Figure A.2: get rid of current line LArIAT HV simple schematics.

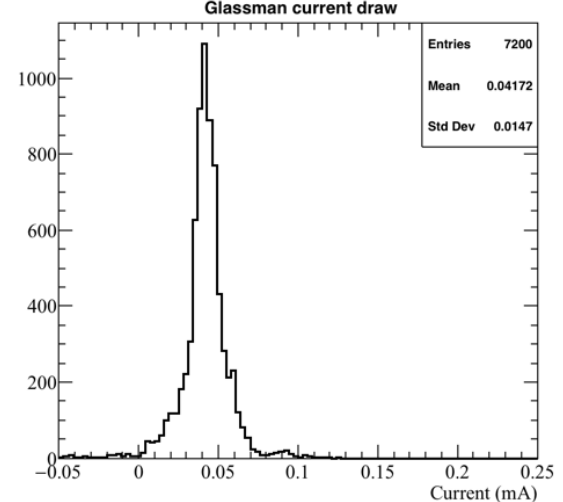


Figure A.3: **the axis is wrong!!** Current reading from the Glassman between May 25th and May 30th, 2016 (typical Run-II conditions).

Using this current, the voltage at the cathode is calculated as

$$V_{BC} = V_{PS} - (I \times R_{eq}) = -23.5 \text{ kV} + (0.00417 \text{ mA} \times 80 \text{ M}\Omega) = -23.17 \text{ kV}, \quad (\text{A.3})$$

where  $I$  is the current and  $R_{eq}$  is the equivalent resistor representing the two filter pots. The electric field, drift voltage, and drift time are then calculated to be

$$E_{\text{field}} = \frac{V_{BC} - V_{\text{shield}}}{\Delta x} = 486.54 \text{ V/cm} \quad (\text{A.4})$$

## E field using cathode-anode piercing tracks

We devise an independent method to measure the drift time (and consequently drift velocity and electric field) using TPC cathode to anode piercing tracks. We use this method as a cross check to the single line method. The basic idea is simple:

0. Select cosmic ray events with only 1 reconstructed track
1. Reduce the events to the one containing tracks that cross both anode and cathode
2. Identify the first and last hit of the track
3. Measure the time difference between these two hits ( $\Delta t$ ).

This method works under the assumptions that the time it takes for a cosmic particle to cross the chamber ( $\sim \text{ns}$ ) is small compared to the charge drift time ( $\sim \text{hundreds of } \mu\text{s}$ ).

We choose cosmic events to allow for a high number of anode to cathode piercing tracks (ACP tracks), rejecting beam events where the particles travel almost perpendicularly to drift direction. We select events with only one reconstructed track to maximize the chance of selecting a single crossing muon (no-michel electron). We utilize ACP tracks because their hits span the full drift length of the TPC, see figure

A.4, allowing us to define where the first and last hit of the tracks are located in space regardless of our assumption of the electric field.

One of the main features of this method is that it doesn't rely on the measurement of the trigger time. Since  $\Delta t$  is the time difference between the first and last hit of a track and we assume the charge started drifting at the same time for both hits, the measurement of the absolute beginning of drift time  $t_0$  is unnecessary. We boost the presence of ACP tracks in the cosmic sample by imposing the following requirements on tracks:

- vertical position (Y) of first and last hits within  $\pm 18$  cm from TPC center (avoid Top-Bottom tracks)
- horizontal position (Z) of first and last hits within 2 and 86 cm from TPC front face (avoid through going tracks)
- track length greater than 48 cm (more likely to be crossing)
- angle from the drift direction (phi in figure A.5) smaller than 50 deg (more reliable tracking)
- angle from the beam direction (theta in figure A.5) grater than 50 deg (more reliable tracking)

Tracks passing all these selection requirements are used for the  $\Delta t$  calculation.

For each track passing our selection, we loop through the associated hits in order to retrieve the timing information. The analysis is performed separately on hits on the collection plane and induction plane, but lead to consistent results. As an example of the time difference, figures A.6 and A.7 represent the difference in time between the last and first hit of the selected tracks for Run-II Positive Polarity sample on the collection and induction plane respectively. We fit with a Gaussian to the peak of the  $\Delta t$  distributions to extract the mean drift time and the uncertainty associated with

it. The long tail at low  $\Delta t$  represent contamination of non-ACP tracks in the track selection. We apply the same procedure to Run-I and Run-II, positive and negative polarity alike.

To convert  $\Delta t$  recorded for the hits on the induction plane to the drift time we utilize the formula

$$t_{drift} = \Delta t - t_{S-I} \quad (\text{A.5})$$

where  $t_{drift}$  is the time the charge takes to drift in the main volume between the cathode and the shield plane and  $t_{S-I}$  is the time it takes for the charge to drift from the shield plane to the induction plane. In Table A.1 we calculated the drift velocity in the S-I region, thus we can calculate  $t_{S-I}$  as

$$t_{S-I} = \frac{l_{S-I}}{v_{S-I}} = \frac{4mm}{1.745mm/\mu s} \quad (\text{A.6})$$

where  $l_{S-I}$  is the distance between the shield and induction plane and  $v_{S-I}$  is the drift velocity in the same region. A completely analogous procedure is followed for the hits on the collection plane, taking into account the time the charge spent in drifting from shield to induction as well as between the induction and collection plane. The value for  $\Delta t_{drift}$ , the calculated drift velocity ( $v_{drift}$ ), and corresponding drift electric field for the various run periods is given in Table A.2 and are consistent with the electric field value calculated with the single line diagram method.

### Delta $t_{drift}$ , drift v and E field with ACP tracks

Data Period	$\Delta t_{Drift}$ [ $\mu s$ ]	Drift velocity [mm/ $\mu s$ ]	E field [V/cm]
RunI Positive Polarity Induction	$311.1 \pm 2.4$	$1.51 \pm 0.01$	$486.6 \pm 21$
RunI Positive Polarity Collection	$310.9 \pm 2.6$	$1.51 \pm 0.01$	$487.2 \pm 21$
RunII Positive Polarity Induction	$315.7 \pm 2.8$	$1.49 \pm 0.01$	$467.9 \pm 21$
RunII Positive Polarity Collection	$315.7 \pm 2.7$	$1.49 \pm 0.01$	$467.9 \pm 21$
RunII Negative Polarity Induction	$315.9 \pm 2.6$	$1.49 \pm 0.01$	$467.1 \pm 21$
RunII Negative Polarity Collection	$315.1 \pm 2.8$	$1.49 \pm 0.01$	$470.3 \pm 21$
Average Values	314.1	$1.50 \pm 0.01$	$474.3 \pm 21$

Table A.2:  $\Delta t$  for the different data samples used for the Anode-Cathode Piercing tracks study.

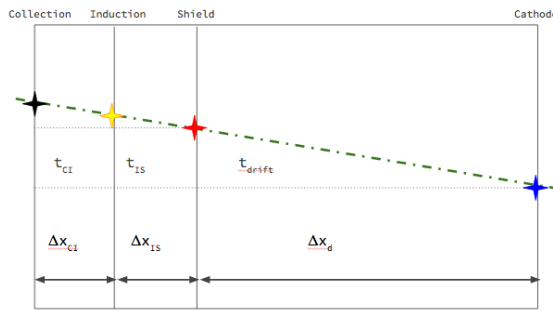


Figure A.4: Pictorial representation of the YX view of the TPC. The distance within the anode planes and between the shield plane and the cathode is purposely out of proportion to illustrate the time difference between hits on collection and induction. A ACP track is shown as an example.

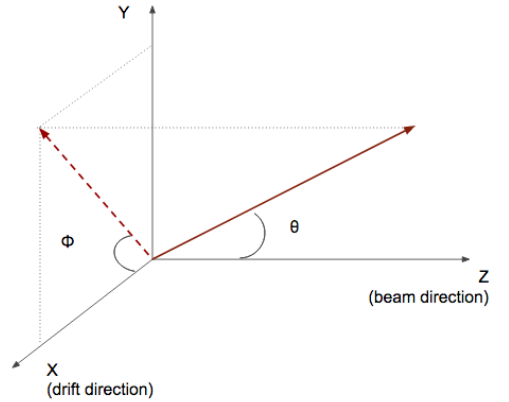


Figure A.5: Angle definition in the context of LArIAT coordinates system.

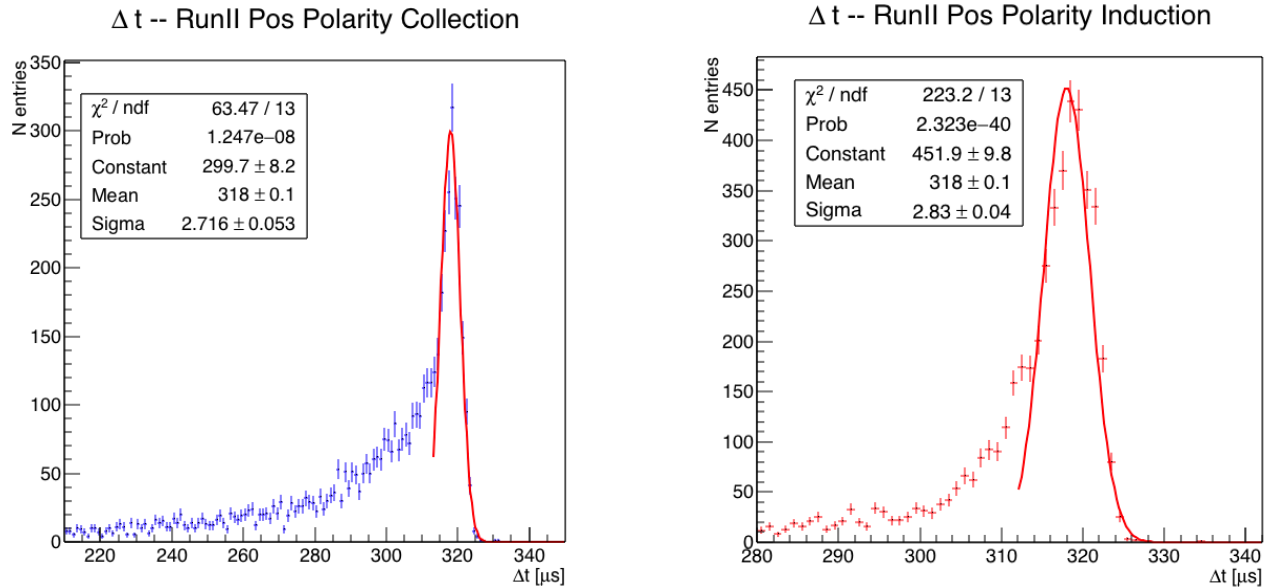


Figure A.6: Collection plane  $\Delta t$  fit for Run II positive polarity ACP data selected tracks.

Figure A.7: Induction plane  $\Delta t$  fit for Run II positive polarity ACP data selected tracks.

# Bibliography

- [1] Precision electroweak measurements on the z resonance. *Physics Reports*, 427(5):257 – 454, 2006.
- [2] R. Acciarri et al. Demonstration and Comparison of Operation of Photomultiplier Tubes at Liquid Argon Temperature. *JINST*, 7:P01016, 2012.
- [3] A. Aguilar-Arevalo et al. Evidence for neutrino oscillations from the observation of anti-neutrino(electron) appearance in a anti-neutrino(muon) beam. *Phys. Rev.*, D64:112007, 2001.
- [4] A. A. Aguilar-Arevalo et al. Improved Search for  $\bar{\nu}_\mu \rightarrow \bar{\nu}_e$  Oscillations in the MiniBooNE Experiment. *Phys. Rev. Lett.*, 110:161801, 2013.
- [5] C. Anderson et al. The ArgoNeuT Detector in the NuMI Low-Energy beam line at Fermilab. *JINST*, 7:P10019, 2012.
- [6] C. Athanassopoulos et al. Evidence for  $\nu(\mu) \rightarrow \nu(e)$  neutrino oscillations from LSND. *Phys. Rev. Lett.*, 81:1774–1777, 1998.
- [7] Borut Bajc, Junji Hisano, Takumi Kuwahara, and Yuji Omura. Threshold corrections to dimension-six proton decay operators in non-minimal {SUSY} su(5) {GUTs}. *Nuclear Physics B*, 910:1 – 22, 2016.
- [8] BASF Corp. 100 Park Avenue, Florham Park, NJ 07932 USA.

- [9] D. V. Bugg, R. S. Gilmore, K. M. Knight, D. C. Salter, G. H. Stafford, E. J. N. Wilson, J. D. Davies, J. D. Dowell, P. M. Hattersley, R. J. Homer, A. W. O'dell, A. A. Carter, R. J. Tapper, and K. F. Riley. Kaon-nucleon total cross sections from 0.6 to 2.65 gev/ *c.* *Phys. Rev.*, 168:1466–1475, Apr 1968.
- [10] A. Cervera, A. Donini, M.B. Gavela, J.J. Gomez Cádenas, P. Hernández, O. Mena, and S. Rigolin. Golden measurements at a neutrino factory. *Nuclear Physics B*, 579(1-2):17–55, jul 2000.
- [11] ATLAS Collaboration. Observation of a new particle in the search for the standard model higgs boson with the ATLAS detector at the LHC. *Physics Letters B*, 716(1):1–29, sep 2012.
- [12] CMS Collaboration. Observation of a new boson at a mass of 125 gev with the cms experiment at the lhc. *Physics Letters B*, 716(1):30 – 61, 2012.
- [13] Savas Dimopoulos, Stuart Raby, and Frank Wilczek. Proton Decay in Supersymmetric Models. *Phys. Lett.*, B112:133, 1982.
- [14] D. Drakoulakos et al. Proposal to perform a high-statistics neutrino scattering experiment using a fine-grained detector in the NuMI beam. 2004.
- [15] A.A. Aguilar-Arevalo et al. The miniboone detector. *Nuclear Instruments and Methods in Physics Research Section A: Accelerators, Spectrometers, Detectors and Associated Equipment*, 599(1):28 – 46, 2009.
- [16] Antonio Bueno et al. Nucleon decay searches with large liquid argon TPC detectors at shallow depths: atmospheric neutrinos and cosmogenic backgrounds. *Journal of High Energy Physics*, 2007(04):041–041, apr 2007.
- [17] C Athanassopoulos et al. The liquid scintillator neutrino detector and LAMPF neutrino source. *Nuclear Instruments and Methods in Physics Research Sec-*

- tion A: Accelerators, Spectrometers, Detectors and Associated Equipment*, 388(1-2):149–172, mar 1997.
- [18] L. Aliaga et al. Minerva neutrino detector response measured with test beam data. *Nuclear Instruments and Methods in Physics Research Section A: Accelerators, Spectrometers, Detectors and Associated Equipment*, 789:28 – 42, 2015.
- [19] M Adamowski et al. The liquid argon purity demonstrator. *Journal of Instrumentation*, 9(07):P07005, 2014.
- [20] H Fenker. Standard beam pwc for fermilab. Technical report, Fermi National Accelerator Lab., Batavia, IL (USA), 1983.
- [21] H Fesbach. Theoretical nuclear physics: Nuclear reactions. 1992.
- [22] J. A. Formaggio and G. P. Zeller. From ev to eev: Neutrino cross sections across energy scales. *Rev. Mod. Phys.*, 84:1307–1341, Sep 2012.
- [23] E. Friedman et al. K+ nucleus reaction and total cross-sections: New analysis of transmission experiments. *Phys. Rev.*, C55:1304–1311, 1997.
- [24] Glassman High Voltage, Inc., Precision Regulated High Voltage DC Power Supply.
- [25] D S Gorbunov. Sterile neutrinos and their role in particle physics and cosmology. *Physics-Uspekhi*, 57(5):503, 2014.
- [26] S. Hansen, D. Jensen, G. Savage, E. Skup, and A. Soha. Fermilab test beam multi-wire proportional chamber tracking system upgrade. June 2014. International Conference on Technology and Instrumentation in Particle Physics (TIPP 2014).
- [27] Peter W. Higgs. Broken symmetries and the masses of gauge bosons. *Physical Review Letters*, 13(16):508–509, oct 1964.

- [28] P.W. Higgs. Broken symmetries, massless particles and gauge fields. *Physics Letters*, 12(2):132–133, sep 1964.
- [29] C. Jarlskog. A basis independent formulation of the connection between quark mass matrices, CP violation and experiment. *Zeitschrift für Physik C Particles and Fields*, 29(3):491–497, sep 1985.
- [30] Ettore Majorana. Teoria simmetrica dell'elettrone e del positrone. *Il Nuovo Cimento*, 14(4):171–184, apr 1937.
- [31] FM Newcomer, S Tedja, R Van Berg, J Van der Spiegel, and HH Williams. A fast, low power, amplifier-shaper-discriminator for high rate straw tracking systems. *IEEE Transactions on Nuclear Science*, 40(4):630–636, 1993.
- [32] Emmy Noether. Invariant variation problems. *Transport Theory and Statistical Physics*, 1(3):186–207, jan 1971.
- [33] S. Pascoli, S.T. Petcov, and A. Riotto. Leptogenesis and low energy cp-violation in neutrino physics. *Nuclear Physics B*, 774(1):1 – 52, 2007.
- [34] C. Patrignani et al. Review of Particle Physics. *Chin. Phys.*, C40(10):100001, 2016.
- [35] B. Pontecorvo. Neutrino Experiments and the Problem of Conservation of Leptonic Charge. *Sov. Phys. JETP*, 26:984–988, 1968. [Zh. Eksp. Teor. Fiz.53,1717(1967)].
- [36] Steve Ritz et al. Building for Discovery: Strategic Plan for U.S. Particle Physics in the Global Context. 2014.
- [37] Sigma-Aldrich, P.O. Box 14508, St. Louis, MO 63178 USA.
- [38] Hermann Weyl. Gravitation and the electron. *Proceedings of the National Academy of Sciences of the United States of America*, 15(4):323–334, 1929.

- [39] C. S. Wu, E. Ambler, R. W. Hayward, D. D. Hoppes, and R. P. Hudson. Experimental test of parity conservation in beta decay. *Phys. Rev.*, 105:1413–1415, Feb 1957.
- [40] T. Yanagida. Horizontal symmetry and masses of neutrinos. *Progress of Theoretical Physics*, 64(3):1103–1105, sep 1980.